Predicting the Influence of Strain on Crack Length Measurements Performed using the Potential Drop Method.

K. M. Tarnowski[1], D. W. Dean[2], K. M. Nikbin[1] and C. M. Davies[1]

[1] Department of Mechanical Engineering, Imperial College London, South Kensington Campus, London, SW7 2AZ. UK.

[2] EDF Energy, Barnett Way, Barnwood, Gloucester, GL4 3RS. UK.

Abstract:

The potential drop (PD) crack growth measurement technique is sensitive to strain accumulation which is often erroneously interpreted as crack extension. When testing ductile materials these errors can be significant, but in many cases the optimum method of minimising or supressing them remains unknown because it is extremely difficult to measure them experimentally in isolation from other sources of error, such non-ideal crack morphology. In this work a novel method of assessing the influence of strain on PD, using a sequentially coupled structural-electrical finite element (FE) model, has been developed. By comparing the FE predictions with experimental data it has been demonstrated that the proposed FE technique is extremely effective at predicting trends in PD due to strain. It has been used to identify optimum PD configurations for compact tension, C(T), and single edge notched tension, SEN(T), fracture mechanics specimens and it has been demonstrated that the PD configuration often recommended for C(T) specimens can be subject to large errors due to strain accumulation. In addition, the FE technique has been employed to assess the significance of strain after the initiation of stable tearing for a monotonically loaded C(T) specimen. The proposed FE technique provides a powerful tool for optimising the measurement of crack initiation and growth in applications where large strains are present, e.g. *J-R* curve and creep crack growth testing.

Keywords: Potential drop method; Crack initiation; Crack growth; Finite element analysis; Deformation

1. Nomenclature

1.1 Symbols

a	Crack length
a_0	Initial crack length
Δa_t	Crack extension due to stable tearing
B	Specimen thickness
B_n	Net specimen thickness
E	Young's modulus
f	Frequency
K_g	Geometric gauge factor
K_m	Material gauge factor
K_{tot}	Total gauge factor
L	Specimen length
ΔR	Change in resistance
R_0	Initial resistance
V	Potential drop
V_0	Initial potential drop
W	Specimen width
δ	Skin depth
ε	Strain
ε_f	Strain at failure
ε_u	Strain at ultimate tensile stress
ε_{xx}	Normal strain parallel to the x axis
ε_{yy}	Normal strain parallel to the y axis
μ	Magnetic permeability
v	Poisson's ratio
$\Delta\rho$	Change in resistivity
ρ_0	Initial resistivity
$\sigma_{0.2}$	0.2% proof stress
σ_u	Ultimate tensile stress

1.2 Acronyms

AC	Alternating Current
ACPD	Alternating Current Potential Drop
CMOD	Crack Mouth Opening Displacement
C(T)	Compact Tension
DC	Direct Current
DCPD	Direct Current Potential Drop

DIC	Digital Image Correlation
EDM	Electrical Discharge Machined
FE	Finite Element
LCF	Low Cycle Fatigue
PD	Potential Drop
SEN(T)	Single Edge Notch Tension

2. Introduction

Accurate laboratory measurements of crack initiation and growth are of vital importance in characterising material behaviour, which is necessary for assessing the residual life of structural components. The Potential Drop (PD) technique is one of the most common methods of performing these measurements in metals. It works on the principle that a constant current flowing through a specimen containing a crack generates an electrical field which is sensitive to changes in the geometry of the specimen, in particular crack extension. As the crack grows the PD, measured between two probes located either side of the crack, will increase. By using a suitable calibration function, this increase in PD can be correlated to crack extension.

It is well known that strain can be a source of error in PD measurements due to a combination of local crack tip blunting [1–3] and global specimen deformation [1,2]. This problem is exacerbated as tougher and more ductile alloys are developed and is of particular concern during the measurement of *J-R* curves [1,2], creep crack growth [3,4] and Low Cycle Fatigue (LCF) crack growth [5] where large inelastic strains (plasticity and/or creep) are present. Another common source of error in PD measurements is crack morphology. Calibration functions are typically derived assuming a planar, continuous, straight fronted crack, but real cracks are rarely so well behaved. Typical departures from this ideal geometry include crack tunnelling [6–8], asperities on the crack faces which provide alternative paths for the electrical current [8] and uncracked islands of material behind the crack tip [3].

To accurately measure crack initiation and growth in the laboratory it is necessary to distinguish the change in PD specifically due to crack growth. This requires an understanding of how other factors, such as strain and crack morphology, influence PD throughout a test. The focus of this work is to determine the influence of strain on PD measurements.

The influence of strain on PD is inherently linked to crack morphology because the strain field in the vicinity of the crack depends on the crack geometry. This prevents the experimental determination of the influence of strain on PD because it is prohibitively difficult to control or measure crack morphology precisely for the duration of a crack growth test. The introduction of side grooves can reduce crack tunnelling, but the other aspects of morphology (described above) cannot be controlled and, although in a few limited cases in-situ measurements of crack morphology have be performed (using X-ray computed tomography [9] or ultrasonics [8]) such measurements are generally unsuitable or impractical for most experimental applications.

Given the limitations of an experimental approach to determining the influence of strain on PD an alternative is required. This paper considers the use of a FE approach where the crack morphology can be prescribed and is therefore known for the duration of the analysis. The influence of strain on PD can therefore be studied in detail as it can be isolated from this influence of crack morphology. The development of this capability is particularly

timely given the ongoing development of a new PD annex for the ASTM fracture toughness standard [10] and a current review of the PD guidance proposed in the ASTM creep crack growth standard [11].

2.1 The PD Technique

There are two main variants of the PD technique: Direct Current Potential Drop (DCPD) and Alternating Current Potential Drop (ACPD). ACPD can be further categorized into low frequency and high frequency. When an Alternating Current (AC) with a sufficiently high frequency passes through a conductor the current density decreases exponentially with distance from the surface [12]. This is known as the 'skin effect'. For analysis purposes this current distribution is often simplified to a uniform current acting over a distance, δ. This is known as the 'skin depth' and is calculated from Equation (1) where ρ is the electrical resistivity of the material, μ is the magnetic permeability of the material and f is the frequency of the applied current. ACPD is considered 'high frequency' when the skin depth is much smaller than the specimen dimensions.

$$\boldsymbol{\delta = \left(\frac{\rho}{\pi f \mu}\right)^2} \quad \textbf{(1)}$$

The electrical resistivity and magnetic permeability of metals are both strain dependent [13–16] so for high frequency ACPD the current distribution is also strain dependent. This results in a complex relationship between strain and PD making it extremely difficult to distinguish the effects of crack growth [13,16].

DCPD is the more common variant of the PD technique. This is mainly due to the simplicity and availability of the equipment [17]. The skin effect does not apply to DC so when the current is passed through a conductor, it tends to fill the specimen limited only by the separation of the current injection points [18]. The PD measurement is therefore independent of the magnetic permeability of the material which simplifies the relationship between strain and PD compared to high frequency ACPD. For this reason DCPD is more commonly used to measure crack extension in ductile materials and is the focus of this paper.

At sufficiently low frequencies the skin depth calculated from Equation (1) becomes much greater than the specimen dimensions and AC behaves in a quasi-DC manner. The frequency at which this occurs is material and geometry dependent. Recently a low frequency ACPD system has been developed which demonstrates reduced noise and increased thermal stability compared to a typical DCPD system [19]. This system has been used to obtain the experimental measurements reported in this paper. Due to the quasi-DC current distribution the results are directly applicable to DCPD.

2.2 The Influence of Strain on DCPD

It is well known that strain can influence PD measurements, for example, it is this phenomenon which is utilized in a typical resistance strain gauge. It is therefore not surprising that strain is often identified as a significant source of error when using the PD technique. The example of a resistance strain gauge is used here to explain the influence of strain on DCPD measurements. It should be noted that the following equations are only valid for small strains, which is typical of a resistance strain gauge operating in the elastic regime, but the general principals apply to larger strains.

2.2.1 A Typical Resistance Strain Gauge

The total gauge factor of a resistance strain gauge, K_{tot}, is the sensitivity of the resistance, R, to the applied uniaxial strain, ε. This is defined by Equation (2) where ΔR is the change in resistance due to strain and R_0 is the resistance of the unstrained gauge [20].

$$\boldsymbol{K_{tot} = \frac{\Delta R / R_0}{\varepsilon}} \tag{2}$$

For gauges manufactured from isotropic materials, this can be written as Equation (3) where ν is the Poisson's ratio and $\Delta\rho$ is the change in electrical resistivity due to strain and ρ_0 is the electrical resistivity of the unstrained gauge.

$$\boldsymbol{K_{tot} = 1 + 2\nu + \frac{\Delta \rho / \rho_0}{\varepsilon}} \tag{3}$$

Alternatively, this can be written as Equation (4) where K_g is the geometric gauge factor associated with a change in physical geometry, and K_m is the material gauge factor associated with a change in electrical resistivity. They are calculated from Equations (5) and (6) respectively.

$$\boldsymbol{K_{tot} = K_g + K_m} \tag{4}$$

$$\boldsymbol{K_g = 1 + 2\nu} \tag{5}$$

$$\boldsymbol{K_m = \frac{\Delta \rho / \rho_0}{\varepsilon}} \tag{6}$$

For most metals in the elastic regime, where the uniaxial deformation of the gauge is due to the distortion of the atomic lattice, the geometric gauge factor, K_g, is approximately 1.6 ($\nu \approx 0.3$). The corresponding material gauge factor, K_m, is typically smaller so the influence of strain on PD is dominated by geometric effects [19] although, for a few materials it can be larger, e.g. Platinum [21]. For metals operating in the plastic regime, where uniaxial deformation of the gauge is due to the introduction of dislocations, the total gauge factor, K_{tot}, is often taken as 2.0, independent of the material [20,22,23]. This is because the influence of dislocation density on resistivity is very small [24] so $K_m \approx 0$ and $K_{tot} \approx K_g$ for incompressible deformation ($\nu = 0.5$).

2.2.2 Predicting the Influence of Strain on PD Measurements Using FE

When using the PD technique to measure crack extension, errors due to strain are only considered significant when large inelastic strains are present, e.g. when measuring of *J-R* curves [1,2], creep crack growth [3,4] or Low Cycle Fatigue (LCF) crack growth [5]. As discussed above, the influence of inelastic strain on PD measurements is predominately geometric in nature and this change in geometry can be easily predicted using a structural FE analysis. By coupling this with an electrical analysis the geometric effects of strain on PD can be predicted and, assuming that any material effects remain secondary, this should provide a good estimate of the total influence of strain on PD.

This analysis technique has already been used to successfully predict the influence of strain on PD measurements performed along the gauge region of uniaxial tensile specimens manufactured from austenitic

type 316L stainless steel [5], X70 pipeline steel and S690 structural steel [25]. Experimental measurements were within 10% of FE predictions and analytical calculations, both of which neglected material effects of strain on PD. This confirms that geometric effects dominate when the entire gauge region is experiencing significant uniaxial plastic deformation.

A limited number of studies have applied the same technique to cracked geometries. Ljustell [5] performed an analysis of a C(T) specimen with a stationary crack and Ke and Stahle [24] performed a similar analysis on a three point bend specimen. Both studies predicted that large plastic strains have a significant influence on PD measurements but neither provided experimental validation of the FE model. Ke and Stahle did however present a qualitative comparison with experimental data which demonstrated consistent trends [24].

This paper investigates the use of a sequentially coupled structural-electrical FE analysis to provide insight into the influence of strain on PD measurements. Three applications of this modelling technique have been considered which provide increasing levels of complexity and the accuracy of the predictions has been assessed by comparison with experimental measurements where appropriate. These three applications are:

1. Uniaxial tensile specimens.
2. Monotonically loaded Compact Tension, C(T), and Single Edge Notched Tension, SEN(T), specimens containing a stationary crack.
3. A monotonically loaded C(T) specimen with a growing crack (stable tearing).

The uniaxial tensile specimens were assessed to demonstrate consistency with previous studies [5,25] and to obtain uniaxial tensile material properties for use in all the FE models. The specimens containing a stationary crack were used to assess the accuracy of the FE analysis for predicting the influence of strain in the presence of a complex strain field by comparison with experimental data. It was also use to identify whether some PD configurations which are less susceptible to the influence of strain than others. Finally, the analysis technique was extended to a growing crack to investigate the influence of strain during crack growth. All tests and analyses were performed using the same ex-service austenitic Type 316H stainless steel. This paper focuses on elastic-plastic deformation, however the analogy between power-law plasticity and power-law creep maybe exploited, and thus the results may also be relevant to creep crack growth.

3. Uniaxial Specimen

A series of uniaxial tensile tests were performed to see if the proposed FE analysis method could predict the change in PD along the gauge region. The results were also compared with data from previous studies [5,25] for consistency. The experimental setup is described in the following sub-section, followed by a summary of the uniaxial tensile material properties which have been used in all of the FE models described in this paper. Details of the corresponding FE analysis are then presented followed by a comparison of the FE predictions with the experimental data and a discussion of results.

3.1 Experimental Setup: Uniaxial Specimen

Nine room temperature uniaxial tensile tests were performed. Five of these tests (Specimen IDs UTT_RB01 to UTT_RB05) were used to obtain mean tensile material properties for use in the FE models and to demonstrate the level of scatter in the material properties. These initial tests did not include PD measurements, unlike the

remaining four tests (Specimen IDs UTT_RB06 to UTT_RB09) which were used to measure the influence of strain on PD for comparison with FE predictions. The specimen geometry is shown in Figure 1 and is in accordance with ASTM E8/E8M-13a [26].

For each specimen an extensometer of gauge length 25.0 mm and a travel of +25.0/-2.5 mm was attached to the central region before it was loaded in displacement control at a cross-head speed of 2 mm/min. A data acquisition rate of 10Hz was applied to all tests.

For specimens UTT_RB01 to UTT_RB05 an additional extensometer was located on the opposite side of the gauge region. The Young's modulus of the material was obtained from the average of the two extensometers in accordance with ASTM E111-04 [27]. For specimens UTT_RB06 to UTT_RB09 a single extensometer was used to provide space for the PD probes which measured the PD over the 25 mm gauge length. The current injection leads were attached to either end of the specimen on the unthreaded section of the grip region 2 mm from the threads. This is sufficiently remote to produce a uniform electrical field in the gauge region. The current injection and PD probe leads were 0.8 mm diameter Chromel wire which was spot welded to the specimen and twisted together to avoid electromagnetic interference. The exterior of the specimen grips was painted to electrically isolate them from the load frame and prevent alternative paths for the current. Electrical isolation was confirmed by ensuring negligible change in the PD measured across the specimen before and after it was inserted into the load frame. The painted surface was also visually inspected after the test to confirm that it remained intact. The experimental setup is shown in Figure 2.

A 3 mA constant current was passed through the specimen at a frequency of 2Hz. This frequency is low enough to produce negligible skin effect for this material and geometry such that the current behaves in a quasi-DC manner. This was confirmed by obtaining PD measurements at a range of frequencies up to 30Hz. These measurements demonstrated no frequency dependency.

3.2 Tensile Material Properties

For all tests, necking and subsequent failure occurred within the 25 mm gauge length. The Young's modulus, E, 0.2% proof stress, $\sigma_{0.2}$, ultimate tensile stress, σ_u, strain at the ultimate tensile stress, ε_u, and failure strain, ε_f, for tests UTT_RB01 to UTT_RB05 are summarised in Table 1. The failure strain is the average engineering strain measured along the gauge length. The mean and standard deviations of all five tests are also provided. The standard deviations are relatively small, demonstrating a high level of repeatability.

Specimen ID	E **[GPa]**	$\sigma_{0.2}$ **[MPa]**	σ_u **[MPa]**	ε_u **[%]**	ε_f **[%]**
UTT_RB01	190.6	313.5	605.7	47.9	64.0
UTT_RB02	196.2	302.5	609.7	49.3	64.9
UTT_RB03	203.2	290.3	604.3	49.1	67.0
UTT_RB04	191.9	291.8	607.9	47.7	63.5
UTT_RB05	194.5	302.9	610.6	51.5	68.8
Mean:	**195.3**	**300.2**	**607.6**	**49.1**	**65.6**
Standard Deviation:	**4.9**	**9.4**	**2.6**	**1.5**	**2.2**

Table 1: Uniaxial tensile material properties for austenitic Type 316H stainless steel at room temperature

The true plastic stress-strain data for the same tests is provided in Figure 3 and again, the results are consistent. The data in this figure is only provided up to 40% strain which corresponds approximately to the true plastic strain at the ultimate tensile stress. Beyond this point material data cannot be easily obtained from a standard uniaxial tensile test so a power-law regression fit between 10% and 40% plastic strain has been used to extrapolate the data for the FE model.

3.3 FE Analysis: Uniaxial Specimen

A 3D quarter model of the specimen was produced using Abaqus v6.13-2 [28], taking advantage of the planes of symmetry, as shown in Figure 4. The model incorporates the unthreaded portion of the grip region to include the current injection location. The mesh consists of 11,180 linear elements. For the structural analysis, reduced integration 8-node brick elements (type C3D8R) were used. These were converted to 8-node thermal-electrical brick elements (type DC3D8E) for the electrical analysis.

For the structural analysis, mean uniaxial material properties from the five tests described above were applied to the model (see Table 1 and Figure 3). The plasticity model implemented in the analysis uses the associated plastic flow rule and the von Mises yield surface. Isotropic hardening was assumed. Symmetry boundary conditions were applied to the *'Y_1'* and *'Z'* planes shown in Figure 4. A displacement boundary condition was applied to all nodes on the *'Y_2'* plane in the positive *y* direction. This displacement was selected to produce an average strain, in the gauge region equal to the average failure strain, ε_f, provided in Table 1.

Large displacement formulation (NLGEOM) was applied to accurately capture the deformed shape. Towards the end of the analysis localised necking occurs at the middle of the gauge length when the inequality in Equation (7), is satisfied. This is achieved by including the sample's grip region in the model such that the von Mises stress along the gauge region is not perfectly uniform. This modelling approach was developed by Brünig [29] and provides a reasonable approximation of the full uniaxial tensile test. To capture the deformation of the necked region the mesh has been refined as shown in Figure 4. It should be noted that if the FE model did not include the change in diameter at the grip region, the von Mises stress would be perfectly uniform along the gauge length so there would be no location for necking to initiate.

$$\boldsymbol{\sigma_{true} > \frac{d\sigma_{true}}{d\varepsilon_{true}}} \tag{7}$$

The deformed shape of the specimen was output from structural analysis at eight increments and an electrical analysis was performed on each of these geometries as well as the undeformed geometry. For each analysis an electrical ground (0 V potential) boundary condition was applied to all nodes on the *'Y_1'* plane and a point current source was applied to the node labelled *'I'*. All other surfaces were assumed to be perfectly insulated. The electrical potential was measured at the node, labelled '*PD*'.

All results presented in this paper are in the form of relative change in PD, $\Delta V/V_0$, where V_0 is the PD for the undeformed geometry and ΔV is the change in PD relative to V_0. In this form the results are independent of the applied current and electrical resistivity so these values can be selected arbitrarily. The only material properties required to generate the FE model are therefore the uniaxial tensile data.

3.4 Results & Discussion: Uniaxial Specimen

The engineering stress-strain data for tests UTT_RB06 to UTT_RB09 are compared in Figure 5. Up to the maximum load, which occurs at an engineering strain of ~50%, all four tests demonstrate consistent behaviour with the exception of a small difference in the yield strength of specimen UTT_RB06. This may be due to slight inhomogeneity of the ex-service material. FE predictions are also provided in the same figure where engineering strain is averaged over the 25 mm gauge length so it is directly comparable to the experimental extensometer data. The predictions are consistent with the experimental observations up to the maximum load, but the two diverge at higher strains. This is probably due to the power-law extrapolation of the material properties and an inability of the FE model to fully capture the deformed shape of the necked region of the FE model.

The relative change in PD, measured experimentally, is compared with the FE predictions in Figure 6. Prior to the maximum load there is good agreement, with the FE consistently slightly lower than the experimental data by <5%. This small difference is most likely caused by strain related changes in material resistivity which are not included in the FE model. Changes in temperature will also influence the material resistivity but this effect should be small due to the closely controlled laboratory temperature and the relatively low loading rate. After the maximum load the FE over-predicts the relative change in PD. This is consistent with the differences in the experimental and predicted stress-strain data beyond maximum load, which are described above. The results in Figure 6 are also consistent with observations made by Ljustell [5] when performing similar tests on austenitic Type 316L stainless steel.

For these uniaxial tensile specimens, the material effects of strain are small compared to the geometric effects and by neglecting them, a sequentially coupled structural-electrical FE model can be used to predict the change PD due to strain with a high degree of accuracy. Additional accuracy may be obtained by performing a reference measurement to suppress any fluctuations in temperature but, for the results presented here, any improvement is likely to be small.

4. Cracked Specimens: Stationary Crack

Uniaxial tensile tests produce a nominally uniform strain field along the gauge length (up to the onset of necking) but when using the PD technique to measure crack growth, the strain field is significantly more complex. To investigate whether the same analysis techniques can successfully predict the influence of strain in such complex strain fields, monotonically loaded specimens containing a stationary crack have been considered. A range of specimen geometries, crack lengths and PD configurations are also considered to determine how these factors influence the relationship between strain and PD. The experimental setup is described in detail in the following sub-section, followed by details of the corresponding FE analyses. The experimental data and the FE predictions are then compared and discussed.

4.1 Experimental Setup: Stationary Crack

Recently a series of room temperature experiments have been performed to investigate the influence of strain on PD for monotonically loaded C(T) and SEN(T) specimens [30]. These two specimen types were selected for their different levels of constraint. A range of PD configurations and crack lengths were considered for each

specimen type. Each specimen was manufactured from the same batch of ex-service Type 316H stainless steel used for the uniaxial tensile specimens discussed above. The crack was simulated using an Electrical Discharge Machined (EDM) slit with a tip radius of 0.15 mm. The use of EDM pre-cracked specimens, rather than fatigue pre-cracked specimens, ensured that the crack geometry was precisely known and could be accurately modelled in FE. Each specimen was loaded until significant plastic deformation occurred, but stopped prior to any stable tearing. This absence of stable tearing was confirmed from the post-test fracture surface.

3D Digital Image Correlation (DIC) was performed on each specimen using a stereo camera system consisting of two 5 megapixel monochrome cameras with 100mm lenses. This system was capable of capturing in-plane and out-of-plane displacements of the specimen surface. Strains calculated from these displacements were used to validate the structural FE models. The surface of the specimen was painted matt black and a high contrast white speckle pattern was applied using an airbrush. The images were post-processed using GOM proprietary software Aramis v6.3.0 [31]. A facet size of 19 pixels with 4 pixel overlap was sufficient to capture the strain field without excessive noise. A single pass of a smoothing algorithm, which averaged the strains over a 3x3 grid of facets, was applied to further reduce the noise without masking the high strain gradient close to the crack tip.

4.1.1 SEN(T) Experimental Setup

Four SEN(T) specimens were tested with different crack lengths. The key dimensions of these specimens are summarised in Table 2. Studs were spot welded onto the front face of each specimen and 'knife edges' were firmly attached to accommodate a clip gauge for the measurement of Crack Mouth Opening Displacement (CMOD). The position of the knife edges was measured before each test so comparable CMOD measurements could be obtained from the FE models.

Specimen ID	a_0/W	a_0 [mm]	W [mm]	B [mm]	L [mm]
CTP_ST30	0.30	7.5	25.0	6.25	50.0
CTP_ST38	0.38	9.5	25.0	6.25	50.0
CTP_ST54	0.54	13.5	25.0	6.25	50.0
CTP_ST70	0.70	17.5	25.0	6.25	50.0

Table 2: Stationary crack SEN(T) specimen key dimensions

The PD configurations used for the SEN(T) specimens are shown in Figure 7. The PD probe locations are labelled with the suffix *'S'* and the current injection locations are labelled with the suffix *'I'*. Four configurations were used to measure the PD across the crack: S_1, S_2, S_3 and S_{tip}. These are shown in Figure 7(a). Each of these configurations used the same current injection location, I. This location produces an approximately uniform current distribution in the gauge region of the specimen. A reference measurement was used to supress any fluctuations in ambient temperature which occur throughout the test. The reference PD probe and current injection locations, S_{ref} and I_{ref} respectively, are shown in Figure 7(b). All of the PD configurations shown in Figure 7 were implemented on each specimen and a multiplexor was used to switch between them but, for clarity, they are shown in separately in this figure.

4.1.2 C(T) Experimental Setup

Two C(T) specimens were tested with different crack lengths typical of fracture toughness testing [10]. The key dimensions of these specimens are summarised in Table 3. 'Knife edges' were machined into the specimen to accommodate a clip gauge along the load-line.

Specimen ID	a_0/W	a_0 [mm]	W [mm]	B [mm]	B_n [mm]
CTP_CT45	0.45	22.5	50.0	25.0	20.0
CTP_CT55	0.55	27.5	50.0	25.0	20.0

Table 3: Stationary crack C(T) specimen key dimensions

The PD configurations considered for the C(T) specimens are shown in Figure 8. The current injection locations are labelled with the suffix *'I'* and the PD probes are labelled with the suffix *'C'*. Figure 8(a) shows PD probe locations C_1, C_3 and C_{tip} where the current is injected at I_1. Figure 8(b) shows PD probe location C_2 where the current is injected at I_2. The reference PD probe and current injection locations, C_{ref} and I_{ref} respectively, are shown in Figure 8(c). All PD configurations shown in Figure 8 were applied to each specimen and a multiplexor was used to switch between them but, for clarity, they are shown in separately in this figure.

4.2 FE Analyses: Stationary Crack

4.2.1 SEN(T) FE Analyses

A quarter model of each SEN(T) specimen was developed using Abaqus v6.13-2 [28]. A 3D model was used to capture the out-of-plane strains. The model for specimen CTP_ST30 ($a/W = 0.3$) is shown in Figure 9. It consists of ~12000 linear brick elements. The structural analysis was performed using reduced integration C3D8R elements and the electrical analysis used DC3D8E thermal-electric elements. Large displacement formulation (NLGEOM) was applied to the structural analysis and a focused mesh was used at the crack tip to accurately capture the strain field. The crack was modelled with a 0.15 mm tip radius, consistent with the EDM slit machined in the specimen. To reduce the computational expense of the analysis only the gauge region of the specimen was modelled.

A displacement boundary condition was applied in the y direction to a reference node located at the centre of the pin hole on the z plane of symmetry. This was transmitted to the gauge region via a kinematic coupling which effectively models the thicker grip region of the specimen as rigid. The reference node was fixed in the x and z directions and prevented from rotating about the x and y axes. It was free to rotate about the z axis to simulate the rotation of the pin on flats in the holes of the shackles which were manufactured in accordance with ASTM E1820-13 [10]. The applied displacement was chosen so the CMOD, measured at the location of the knife edges, matched the values measured experimentally.

For the electrical analyses a ground (0 V potential) boundary condition was applied to the ligament ahead of the crack tip and a uniform unit current (1A) was applied to the top surface of the specimen. All other surfaces were assumed to be perfectly insulated. The electrical potential was measured at nodes located at the PD probe locations shown in Figure 7.

4.2.2 C(T) FE Analyses

Quarter models of both C(T) specimens were developed using Abaqus v6.13-2 [28]. The model for specimen CTP_CT45 ($a/W = 0.45$) is shown in Figure 10. It consists of ~45000 linear elements. The side-grooves were modelled as perfectly sharp to simplify the mesh and a sensitivity study was performed which confirmed that this did not significantly influence the PD response. The pin was explicitly modelled to capture the strain around the pin hole. It was assumed rigid and contact between the pin and the specimen was modelled as 'rough' for simplicity. To assist with model convergence, contact stabilization was included. Checks were performed to confirm that the stabilization energy remained small compared to the total strain energy in the model.

A displacement boundary condition was applied to the pin in the y direction and it was free to rotate about the z axis. It was fixed in the x and z directions and prevented from rotating about the x and y axes. The applied displacement was chosen so the CMOD, measured at the location of the knife edges, matched the values measured experimentally. For each increment the deformed shape was used to perform two separate electrical analyses, one for each of the current injection locations shown in Figure 8.

For the electrical analyses a ground (0 V potential) boundary condition was applied to all nodes on the ligament ahead of the crack tip and a point source unit current (1A) was applied to a node at the relevant current injection location. All other surfaces were assumed to be perfectly insulated. The electrical potential was measured at nodes located at the PD probe locations shown in Figure 8.

4.3 Results: Stationary Crack

4.3.1 SEN(T) Results

To validate the structural model, the experimental load-displacement curves were compared with the FE results. The surface strain fields from DIC were also compared to the FE models for the final displacement increment. These comparisons are provided in Figure 11 for specimen CTP_ST30 ($a/W = 0.30$). There is excellent agreement between the experimental and FE results which provides confidence in the structural model and the tensile material properties. Similar results were obtained for all SEN(T) specimens.

Figure 12 shows the relative change in PD with CMOD for all four SEN(T) specimens. Experimental data, shown by the dashed lines and hollow symbols, is compared with FE predictions, shown by the solid lines and solid symbols. There is a strong correlation between the FE and the experimental data although the FE consistently under-predicts the relative change in PD. The majority of this discrepancy occurs at low values of CMOD. At the termination of the tests this discrepancy is typically 10 to 20%.

The relative change in PD with CMOD is larger when the PD probes are closest to the crack tip but these configurations are also more sensitive to crack extension. To investigate the influence of strain on the corresponding crack length measurement the relative change in PD must be converted to an 'equivalent crack extension'. This is the crack extension which would produce the same relative change in PD and is calculated using the calibration functions provided in [30] and shown in Figure 13. The 'equivalent crack extension' may alternatively be considered as the potential error in the measurement of crack extension due to strain.

Figure 13 demonstrates that for small crack lengths the PD probes should be located close to the plane of the crack to reduce the equivalent crack extension associated with strain. For $a/W = 0.3$, the equivalent crack extension for PD configuration S_3 is approximately double that of S_{tip} but for larger crack lengths, e.g. $a/W = 0.7$, the equivalent crack extension is approximately the same for all PD configurations. These trends are discussed in more detail in the original experimental paper [30] but the key observation from Figure 13 is that the experimentally observed trends are consistently predicted by the FE model. The proposed FE analysis technique therefore provides a method of optimising the experimental setup to reduce the equivalent crack extension due to strain.

4.3.2 C(T) Results

The experimental load-displacement curves for the C(T) specimens are compared to the FE predictions in Figure 14. The FE consistently over-predicts the stiffness of the specimen compared to the experimental data for both specimens. A series of FE sensitivity studies were performed to investigate the source of this discrepancy. The results were relatively insensitive to mesh size, pin flexibility, crack tip acuity and side-groove acuity. The results were sensitive to the method of modelling the pin/hole interaction however, the proposed boundary condition with a rough interface and a pin which is free to rotate is the most flexible so any modifications would only increase the difference between the FE and experimental results. The source of the discrepancy in Figure 14 may therefore be due to inhomogeneity in the ex-service material.

Figure 15 compares the experimental surface strain fields, obtained by DIC, with the FE predictions for the final displacement increment of C(T) specimen CTP_CT45 ($a/W = 0.45$). The lack of DIC data close to the plane of the crack is due to the presence of side-grooves. Away from this region the strains predicted by the FE are lower than those measured experimentally, but the difference is small. This suggests that for a given value of CMOD the FE should be able to predict the influence of strain on PD with a reasonable degree of accuracy, despite the differences observed in Figure 14.

Figure 16 shows the relative change in PD with CMOD for both C(T) specimens. Similar to the SEN(T) specimens there is a strong correlation between the FE and the experimental data with the FE consistently under-predicting the relative change in resistance. The majority of this discrepancy again occurs at low values of CMOD. At the end of the tests this discrepancy is typically 15 to 30% which is slightly larger than discrepancy observed for the SEN(T) specimens. The differences between the FE and experimental strain fields identified in Figure 15 are likely to account for at least some of this additional discrepancy.

The relative change in PD has been converted into a ‘equivalent crack extension’, using the calibration functions provided in [30], and is presented in Figure 17. The experimentally observed trends are again consistently predicted by the FE analyses. The equivalent crack extension for PD configuration C_1 is much higher than the other three configurations, particularly for $a/W = 0.45$. It has been suggested that this may be due to large strains around the pin hole, particularly in the thin section between the pin hole and the machined notch [30]. This hypothesis can be easily investigated using the proposed FE analysis technique, as demonstrated here.

The FE model for specimen CTP_CT45 ($a/W = 0.45$) was re-run with a modified displacement boundary condition. The rigid pin was removed and the displacement was applied to a node at the centre of the hole. This was transferred to all of the nodes on the circumference of the loading hole via a kinematic coupling similar to

that used for the SEN(T) specimens. This prevented the hole from deforming on loading. The node to which the displacement boundary condition was applied was free to rotate about the z axis to simulate pin rotation. The results for the original and modified FE models are shown in Figure 18(a) and (b) respectively.

The modified boundary condition removes the plastic strain around the hole whilst maintaining the strain field around the crack tip. This reduces the equivalent crack extension for PD configuration C_1 to a similar level as the other configurations. The influence on the other PD configurations is negligible. This demonstrates that plastic deformation around the loading hole can have a significant influence on crack extension measurements performed using PD configuration C_1.

4.4 Discussion: Stationary Crack

The results presented here demonstrate that the proposed FE analysis technique is extremely effective at predicting trends in PD due to strain. This powerful capability is ideal for optimising the experimental setup to minimise the influence of strain on PD measurements using relatively low cost FE parametric studies. In this work it has been used to identify PD configurations for SEN(T) and C(T) specimens which are less susceptible to errors in the measurement of crack extension due to strain.

The results presented here are of specific interest for fracture toughness testing where the onset of stable tearing is often identified from an increase in gradient on a plot of PD vs. CMOD [32]. A major limitation of this approach is that for some high toughness, high tearing resistance and high strain hardening materials this change in slope can be extremely subtle which prevents the accurate measurement of crack initiation [33]. Assuming that the gradient on a plot of PD vs. CMOD, after crack initiation, is dominated by crack growth, it is unlikely to be significantly influenced by strain, but prior to crack initiation the gradient is entirely due to strain. Selecting a PD configuration which is less susceptible to the influence of strain will therefore reduce the gradient prior to crack initiation and increase the differential in gradient at the point of crack initiation. This will improve the accuracy of the measurement of crack initiation. For this reason PD configuration C_1 (see Figure 8) should be avoided for C(T) specimens despite being the PD configuration often recommended in fracture toughness standards e.g. [32].

Although the proposed FE analysis technique is extremely effective at predicting trends in PD due to strain, it does not accurately predict the magnitude of the change in PD. The results for the SEN(T) specimens, suggest that this discrepancy is most likely related to the electrical FE model since the structural FE model demonstrates excellent agreement with the experimental data. The majority of the discrepancy also occurs at small values of CMOD when the specimen deformation is predominately elastic which suggests it is most likely related to elastic strain. The most likely cause of the discrepancy between the experimental measurements and FE predictions is therefore a change in the resistivity of the material due to elastic strain which is not captured in the FE model.

The inability of the FE model to predict the magnitude of the change in PD demonstrates that it is not suitable for directly correcting experimental PD data for the influence of strain. Introducing strain dependent electrical material properties into the model could improve the accuracy of the predictions, but this would greatly increase the complexity of the model and the benefits of doing so are somewhat limited. As discussed in the introduction, the influence of strain is inherently linked to the crack morphology. To directly correct

experimental PD data would therefore require the FE model to include the precise evolution of crack morphology and this is extremely difficult to determine experimentally. The addition of strain dependent electrical material properties has therefore not considered further in this study.

5. Cracked Specimen: Growing Crack

After the onset of crack growth, the influence of strain on PD measurements is often ignored. This is assumption is typically based on "engineering judgement", e.g. [2], and is extremely difficult to validate experimentally because, as discussed in the introduction, additional errors associated with the non-ideal morphology of real cracks make it extremely difficult to isolate the influence of strain on PD. In the following section the sequentially coupled structural-electrical FE analysis technique described above has been extended to investigate the influence of strain on PD during growing crack.

By prescribing ideal crack morphology in the analysis, it is removed as a source of error in the measurement of crack extension. The influence of stain on PD can therefore be isolated by comparing the actual crack extension modelled in the analysis to the crack extension predicted from the PD data obtained from the same analysis. Any difference must therefore be the error due to strain. This is a qualitative analysis, rather than quantitative, because, as demonstrated in the previous section, the FE under-predicts the influence of strain on PD. Despite this limitation, this remains a powerful tool for investigating whether these errors associate with strain after the onset of crack growth are significant.

The analysis presented here simulates the stable tearing of a monotonically loading C(T) specimen manufactured from the same ex-service type 316H material used throughout this study. To ensure that the strain in the FE model was representative of a real test, the boundary conditions were determined from experiment. The setup used to derive these boundary conditions is described in the following sub-section followed by details of the FE model and a discussion of the results.

5.1 Experimental Setup: Growing Crack

A stable tearing crack growth test (a *J-R* curve test) was performed to determine a typical relationship between CMOD and crack extension for a C(T) specimen manufactured from ex-service type 316H material. This experimental data was used to define a representative boundary condition for the FE model presented in the following sub-section.

Specimen ID	a_0 [mm]	W [mm]	B [mm]	B_n [mm]
JIC_CT01	23.1	50.0	25.0	17.5

Table 4: Growing crack C(T) specimen key dimensions

A C(T) specimen with similar geometry to that described in the previous section (for a stationary crack) was used to perform this test. The main difference was the addition of a fatigue pre-crack rather than an EDM slit to provide a real crack. A 20 mm long EDM pre-crack (0.15 mm tip radius) was machined into the specimen and extended a further 3.1 mm by fatigue using a sinusoidal load with a peak of 12 kN (K = 18.5 MPa√m), an R-ratio of 0.1 and a loading frequency of 25 Hz. This fatigue pre-cracking was performed on a plane-sided

specimen before side-grooves were machined into the specimen. The key dimensions of the specimen are summarised in Table 4.

The testing procedure was similar to that presented in the previous section with the specimen monotonically loaded in displacement control at a cross-head speed of 2 mm/min, but this test was only terminated after significant stable tearing was observed. PD configurations C_2 and C_{ref}, shown in Figure 8, were implemented. Figure 19 provides a plot of PD vs. CMOD obtained from this test. This figure was used to determine the relationship between CMOD and crack length that was used to derive boundary conditions for the FE model. This relationship was obtained from Figure 19 using the procedure in ISO 12135:2002 [32] and briefly described here.

The onset of stable tearing is identified from the point at which the plot of PD vs. CMOD deviates from the initial linear trend. The PD at this point corresponds to V_0. The solid data points in Figure 19, where $V \leq V_0$, correspond to crack blunting and the dashed line represents a linear regression performed on this data. The hollow data points, where $V > V_0$, correspond to stable tearing. For each of the hollow data points the extent of stable tearing was calculated using the calibration function provided in Equation (8). This equation was derived using FE analysis and details of this derivation are provided in the following sub-section.

$$\frac{a}{W} = 0.0320\left(\frac{V}{V_0}\right)^3 - 0.2331\left(\frac{V}{V_0}\right)^2 + 0.7578\left(\frac{V}{V_0}\right) - 0.0947 \quad (8)$$

After the test, the fracture surface was heat tinted at 300 ºC for 30 minutes and, after the specimen had been allowed to cool, it was sectioned by EDM, as shown in Figure 20. The three slices were polished to reveal the crack profile at the mid-plane and at 2.5 mm and 5.0 mm from the mid-plane, as shown in Figure 21. The remaining specimen was fatigued open to reveal the fracture surface, as shown in Figure 22. To validate the PD measurements, the final crack extension predicted from the PD was compared to the average crack extension measured optically from the post-test fracture surface. The latter was calculated from the area of the crack and the net section thickness which were measured using image processing software, ImageJ [34].

The final crack extension predicted from the PD technique was 2.1 mm whilst the average crack extension measured from the post-test fracture surface was 2.4 mm. This difference of 12.5% is within the permissible 15% discrepancy typical of fracture toughness testing, e.g. ASTM E1820 [10]. This provides confidence that the PD measurements are approximately correct and are adequate for the purposes of generating a representative boundary condition for use in the FE model.

The discrepancy between the PD prediction and post-test fracture surface measurement is most likely due to a combination of plastic strain and non-ideal crack morphology. The non-ideal crack morphology can be observed in both Figure 21 and Figure 22. Ligaments of uncracked material behind the crack tip can be observed in Figure 21, whilst in Figure 22 it is apparent that the crack extension is not perfectly uniform along the crack front. These will both be a source of error in the PD measurements, which demonstrates why it is so difficult to isolate the influence of strain on PD experimentally and confirms the requirement for an alternative approach.

Figure 23 provides the experimentally determined relationship between stable tearing vs. CMOD obtained. This was used determine the boundary conditions for the FE model described in the following sub-section to ensure

that the model included representative levels of strain at each crack increment. Crack growth was incorporated into the FE model in 0.1 mm increments so the actual boundary conditions applied to the model, also shown in Figure 23, demonstrate discrete 0.1 mm steps.

5.2 FE Analysis: Growing Crack

A 3D ¼ model of the C(T) specimen geometry provided in Table 4 was produced using Abaqus v6.13-2 [28]. The side-grooves were modelled as perfectly sharp to simplify the mesh. The mesh in the region of the crack plane was refined to a uniform element size of 0.1 mm to allow small, uniform increments of crack extension. The crack tip was modelled as infinitely sharp. The specimen mesh is shown in Figure 24 and the region of refined mesh is shown in Figure 25. The model consisted of 42,177 linear brick elements.

An initial electrical analysis was performed on this mesh, without any applied load, to derive the calibration function provided in Equation (8). In this analysis a point source unit current (1A) was applied to a node at the current injection location and a ground (0V potential) boundary condition was applied to the ligament ahead of the crack. All other surfaces were assumed to be perfectly insulated. Crack extension was simulated in 0.1 mm increments by progressively releasing lines of nodes, parallel to the original crack front, from the ligament boundary condition. A total of 2.1 mm of crack extension was simulated to correspond with Figure 23. By plotting the normalised PD (V/V_0) obtained from a node at probe location C_2 (see Figure 8) against normalised crack length (a/W) and performing third order polynomial regression on the data, Equation (8) was derived. This typical method of deriving a calibration function does not account for the influence of strain on PD.

After deriving the calibration function, a sequentially coupled structural-electrical analysis was performed on the same geometry to assess the influence of strain on PD. For the structural analysis appropriate boundary conditions were applied to the planes of symmetry and a displacement was applied to a node at the centre of the loading hole. This was transmitted to all of the nodes on the circumference of the loading hole using a kinematic coupling which avoids the computational expense of modelling contact between the loading pin and the hole. This simplified boundary condition does not significantly influence the PD response for configuration C_2, as demonstrated in Figure 18.

The symmetry boundary condition applied to the remaining ligament ahead of the crack tip was modified to simulate 0.1 mm increments of crack extension by releasing a line of nodes parallel to the original crack front. These nodes were released such that the FE model replicated the empirical relationship between stable tearing and CMOD provided in Figure 23. Each 0.1 mm crack increment was modelled as a separate load step. In the coupled electrical analyses the ground (0 V potential) boundary condition applied to the remaining ligament was updated to reflect the extent of crack growth.

For each load step the PD obtained from the electrical analysis was used to predict the crack length using Equation (8). This was compared to the average crack length in the model to identify the influence of strain on the PD predictions. The average crack extension was calculated from the total area of the crack divided by the net section thickness, B_n, at the crack tip. The total area of crack and the net section thickness were both measured from the deformed geometry. This method is consistent with typical measurements performed on the post-test fracture surface and is generally recognised as the most accurate method of determining crack extension. The benefit of an FE analysis is that this procedure can be performed for each crack increment and

not just at the end of the test. It should be noted that the actual increments of crack growth calculated using this method are slightly smaller than 0.1 mm because of the deformation of the specimen.

5.3 Results & Discussion: Growing Crack

The PD vs. CMOD response of the FE model is provided in Figure 26. During the crack blunting phase of the analysis where the crack is stationary (the solid symbols), the relationship between PD and CMOD is approximately linear as demonstrated by the linear regression to the data (the dashed line). During the crack growth phase of the analysis (the hollow symbols) the data departs from this linear trend. This is consistent with the experimental data (Figure 19) and again demonstrates the ability of the FE analysis to predict the trends in PD which are observed experimentally.

Comparing Figure 26 with Figure 19, it is apparent that the FE analysis under-predicts the relative change in PD during blunting compared with the experimental data by ~45%. This is larger than the 15 to 30% discrepancy identified from the stationary crack analysis performed on a C(T) specimen in the previous section. To investigate if this is related to crack tip mesh a sensitivity study was performed reducing the uniform element size at the crack tip from 0.1 mm to 0.02 mm. No significant change in the FE results was observed so the additional discrepancy is therefore most likely due to the non-ideal crack geometry in the experiment.

The stationary crack experiments, discussed in the previous section, were performed on specimens containing an EDM slit rather than a fatigue pre-crack. An EDM slit has a straight crack front and a known crack tip radius which was accurately captured in the FE models so crack morphology was not a source of discrepancy for the stationary crack. The morphology of a fatigue pre-crack however is not so ideal. As observed from Figure 22 the crack front is not perfectly straight, unlike in the crack in the FE model, so this will be a source of discrepancy. Furthermore, it is well known that the faces of a fatigue crack can remain in contact at low loads which provides an alternative path for the electrical current e.g. [35]. As the load increases, the crack faces will separate causing a further increase in PD on top of any changes associated with strain. This behaviour is not captured in the FE model so, for a fatigue pre-crack, a larger change in PD is expected in the experimental data. Despite these discrepancies the FE model described here can still be used to provide a qualitative assessment of the influence of strain on PD during crack growth as discussed here.

The predicted crack extension (from the PD) is compared to the actual crack extension in the model in Figure 27. In this figure the solid line represents a 1:1 ratio (i.e. zero error in the predicted crack extension) and the dashed lines represent ±10% error in the predicted crack extension. In general the crack extension predicted from the PD is in good agreement with the actual crack extension modelled in the analysis although it does slightly over-predict crack extension. This is consistent with the results for the stationary crack where the strain associated with a monotonically increasing load caused an increase in PD. The maximum error in the measurement of crack extension observed in the FE analysis is <5%. The actual experimental error is likely to be somewhat larger because the FE model will under-predict the influence of strain on PD but, even if the FE predictions are out by a factor of 2, it can still be concluded that the influence of strain on PD is relatively small after the onset of crack growth. Therefore the common assumption that the influence of strain on PD is negligible is reasonable for the case considered here. For other combinations of specimen geometry and

material the influence of strain may be more significant but the FE analysis technique presented here provides a relatively simple method of assessing this.

The ability to capture the increase in gradient at the onset of crack growth (Figure 26) presents further opportunities for this FE analysis technique. This capability is of great potential benefit to the measurement of creep crack initiation where strain is known to be a source of significant error [36]. At the present time, there is no accepted method for differentiating between the influence of creep strain during incubation and the onset of creep crack growth. The FE analysis technique described here provides a simple method for investigating whether a similar increase in gradient may be observed during creep crack growth. This will be the subject of future research.

6. Conclusions

A sequentially coupled structural-electrical FE analysis provides a powerful tool to help interpret PD measurements of crack extension in the presence of large strains. This technique only requires the material properties necessary to predict the deformed shape of the specimen, making it extremely simple to implement. The precise control of other parameters which can also affect the PD response (e.g. crack morphology, PD probe location, temperature distribution etc.) allows the influence of strain to be studied in isolation. The same level of control cannot be obtained experimentally.

The proposed analysis technique under-predicts the change in PD due to strain because it does not capture material effects, e.g. changes in resistivity. This can result up to a 30% discrepancy between the FE predictions and experimental data but despite this limitation, the analysis technique is extremely effective at predicting trends in PD due to strain. This is a powerful capability for performing qualitative comparison studies to optimise the experimental setup and to review key assumptions in the interpretation of experimental data. Introducing strain dependent electrical material properties into the model could improve the accuracy of the predictions, but this would greatly increase the complexity of the model without a significant improvement in the overall functionality.

In this study the proposed analysis technique has been used to identify PD configurations for SEN(T) and C(T) specimens which minimise the error in the measurement of crack extension due to strain. These configurations are of particular interest for fracture toughness testing because implementing them will increase range of materials for which the onset of crack growth can be successfully identified from a plot of PD vs. CMOD. It is of particular note that a C(T) specimen with PD probes located on the opposite side of the loading holes to the crack tip is particularly prone to strain related errors, despite this being the recommended configuration in some fracture toughness testing standards.

The analysis technique has also been used to confirm that the influence of strain on PD after the onset of stable tearing is small for a monotonically loaded C(T) specimen manufactured from Type 316H stainless steel. This is extremely difficult to demonstrate experimentally because it is not possible to isolate the influence of strain on PD from other factors such as crack morphology. The analysis presented here could easily be extended to other materials and specimen geometries. It could also be extended to other deformation mechanisms such as creep.

7. Acknowledgements

The authors would like to acknowledge the Engineering and Physical Sciences Research Council (EPSRC), UK for the support under grant EP/I004351/1. This paper is published with permission of EDF Energy Nuclear Generation Ltd.

8. References

[1] Lowes JM, Fearnehough GD. The Detection of Slow Crack Growth in Crack Opening Displacement Specimens Using an Electrical Potential Method. Eng Fract Mech 1971;3:103–4. doi:10.1016/0013-7944(71)90002-6.

[2] Bakker A. A DC Potential Drop Procedure for Crack Initiation and R-Curve Measurements During Ductile Fracture Tests. ASTM STP 856 1985:394–410. doi:10.1520/STP34537S.

[3] Freeman BL, Neate GJ. The Measurement of Crack Length During Fracture at Elevated Temperatures Using the D. C. Potential Drop Technique. In: Beevers CJ, editor. Meas. Crack Length Shape Dur. Fract. Fatigue, Engineering Materials Advisory Services Ltd.; 1980.

[4] Saxena A. Electrical Potential Technique for Monitoring Subcritical Crack Growth at Elevated Temperatures. Eng Fract Mech 1980;13:741–50. doi:10.1016/0013-7944(80)90005-3.

[5] Ljustell P. The Effect of Large Scale Plastic Deformation on Fatigue Crack Length Measurement with the Potential Drop Method. J Test Eval 2011;39:985–1002. doi:10.1520/JTE103532.

[6] Riemelmoser FO, Weinhandl H, Kolednik O, Pippan R. The influence of irregularities in the crack shape on the crack extension measurement by means of the direct-current-potential-drop method. J Test Eval 1999;27:42–6.

[7] Hollstein T, Blauel JG, Voss B. On the Determination of Elastic-Plastic Fracture Material Parameters: A Comparison of Different Test Methods. Elastic-Plastic Fract Test Methods User's Exp ASTM STP 856 1985:104–16.

[8] McIntyre P, Priest AH. Measurement of Sub-Critical Flaw Growth in Stress Corrosion, Cyclic Loading and High Temperature Creep by the DC Electrical Resistance Technique, Report: MG/54/71. 1971.

[9] Steuwer A, Edwards L, Pratihar S, Ganguly S, Peel M, Fitzpatrick ME, et al. In situ analysis of cracks in structural materials using synchrotron X-ray tomography and diffraction. Nucl Instruments Methods Phys Res Sect B Beam Interact with Mater Atoms 2006;246:217–25.

[10] ASTM E1820-15. Standard Test Method for Measurement of Fracture Toughness 2015.

[11] ASTM E1457-15. Standard Test Method for Measurement of Creep Crack Growth Times in Metals 2015.

[12] Paul CR, Nasar SA. Introduction to Electromagnetic Fields. Second Edi. McGraw-Hill; 1987.

[13] Okumura N, Venkatasubramanian T V, Unvala BA, Baker TJ. Application of the AC Potential Drop Technique to the Determination of R Curves of Tough Ferritic Steels. Eng Fract Mech 1981;14:617–25. doi:10.1016/0013-7944(81)90048-5.

[14] Venkatsubramanian T V, Unvala BA. An AC Potential Drop System for Monitoring Crack Length. J Phys E 1984;17:765–71. doi:10.1088/0022-3735/17/9/012.

[15] Marandet B, Sanz G. Experimental Verification of the JIC and Equivalent Energy Methods for the Evaluation of the Fracture Toughness of Steels. ASTM STP 631 1977:462–76. doi:10.1520/STP35555S.

[16] Gibson GP. The use of Alternating Current Potential Drop for Determining J-Crack Resistance Curves. Eng Fract Mech 1987;26:213–22. doi:10.1016/0013-7944(87)90198-6.

[17] Wilkowski GM, Maxey WA. Review and Applications of the Electronic Potential Method for Measuring Crack Growth in Specimens, Flawed Pipes and Pressure Vessels. ASTM STP 791 1983;2:266–94.

[18] Madhi E, Sposito G, Davies CM, Cawley P, Nagy PB. In-Situ Creep Monitoring Using The Potential Drop Method. AIP Conf. Proc., vol. 1335, San Diego, USA: 2010, p. 1631–8. doi:10.1063/1.3592124.

[19] Madhi E, Nagy PB. Sensitivity Analysis of a Directional Potential Drop Sensor for Creep Monitoring. NDT E Int 2011;44:708–17. doi:10.1016/j.ndteint.2011.08.001.

[20] Arlt G. The Sensitivity of Strain Gauges. J Appl Phys 1978;49:4273–4. doi:10.1063/1.325344.

[21] Sciammarella CA, Sciammarella FM. Experimental Mechanics of Solids. Wiley-Blackwell; 2012.

[22] Neubert HKP. Strain Gauges Kinds and Uses. Macmillan & Co. Ltd.; 1967.

[23] Hannah RL, Reed SE. Strain Gauge User's Handbook. Elsevier Science Publishers Ltd.; 1992.

[24] Ke Y, Ståhle P. Crack Length Measurements with a Potential Drop Method: A Finite Element Simulation. Int J Numer Methods Eng 1993;36:3205–20. doi:10.1002/nme.1620361809.

[25] Brinnel V, Döbereiner B, Münstermann S. Characterizing Ductile Damage and Failure: Application of the Direct Current Potential Drop Method to Uncracked Tensile Specimens. Procedia Mater Sci 2014;3:1161–6. doi:10.1016/j.mspro.2014.06.189.

[26] ASTM E8/E8M-13a, Standard Test Methods for Tension Testing of Metallic Materials 2013.

[27] ASTM E111-04, Standard Test Method for Young's Modulus, Tangent Modulus, and Chord Modulus 2004.

[28] ABAQUS v6.13-2, Dassault Systèmes, Vélizy-Villacoublay, France 2013.

[29] Brünig M. Numerical Analysis and Modeling of Large Deformation and Necking Behavior of Tensile Specimens. Finite Elem Anal Des 1998;28:303–19. doi:10.1016/S0168-874X(97)00042-5.

[30] Tarnowski KM, Davies CM, Dean DW, Nikbin KM. The Influence of Plasticity on Crack Length Measurements Using the Potential Drop Technique. ASTM STP 1584 2014:73–96. doi:10.1520/STP158420140055.

[31] Aramis v6.3.0, GOM mbH, Braunschweig, Germany 2013.

[32] ISO 12135:2002. Metalic Materials - Unified Method of Test for the Determination of Quasistatic Fracture Toughness 2002.

[33] Bicego V, Liviero D, Fossati C, Lucon E. JR Curve Testing Utilizing the Reversing Direct Current Electrical Potential Drop Method. ASTM STP 1092 1990:143–66. doi:10.1520/STP25036S.

[34] ImageJ v1.48, National Institute of Health, USA 2013.

[35] Hartman GA, Johnson DA. D-C Electric-Potential Method Applied to Thermal/Mechanical Fatigue Crack Growth. Exp Mech 1987;27:106–12. doi:10.1007/BF02318872.

[36] Webster GA, Ainsworth RA. High temperature Component Life Assessment. Chapman and Hall; 1994.

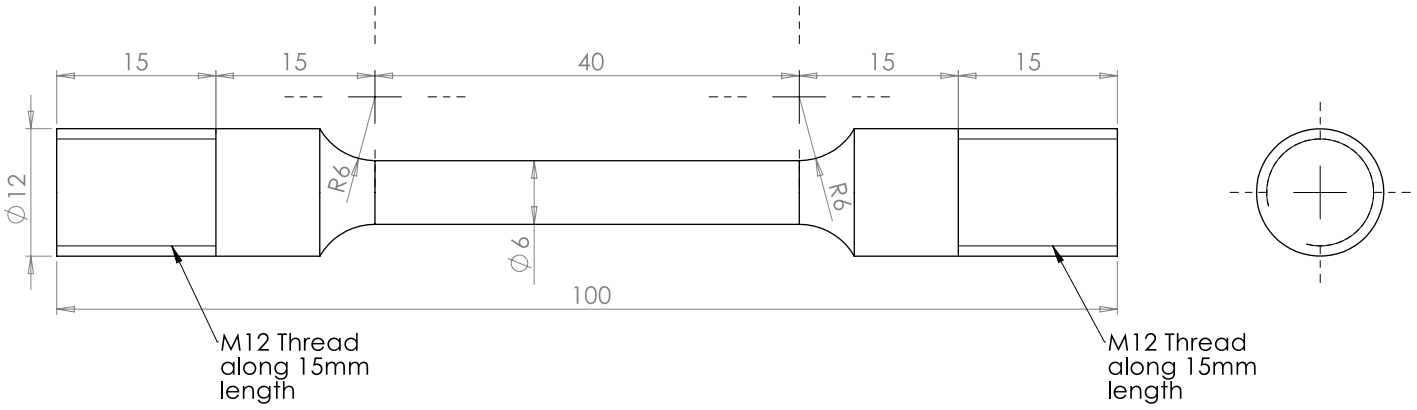
15
15
40
15
15
ϕ12
R6
R6
ϕ6
100
M12 Thread
along 15mm
length
M12 Thread
along 15mm
length

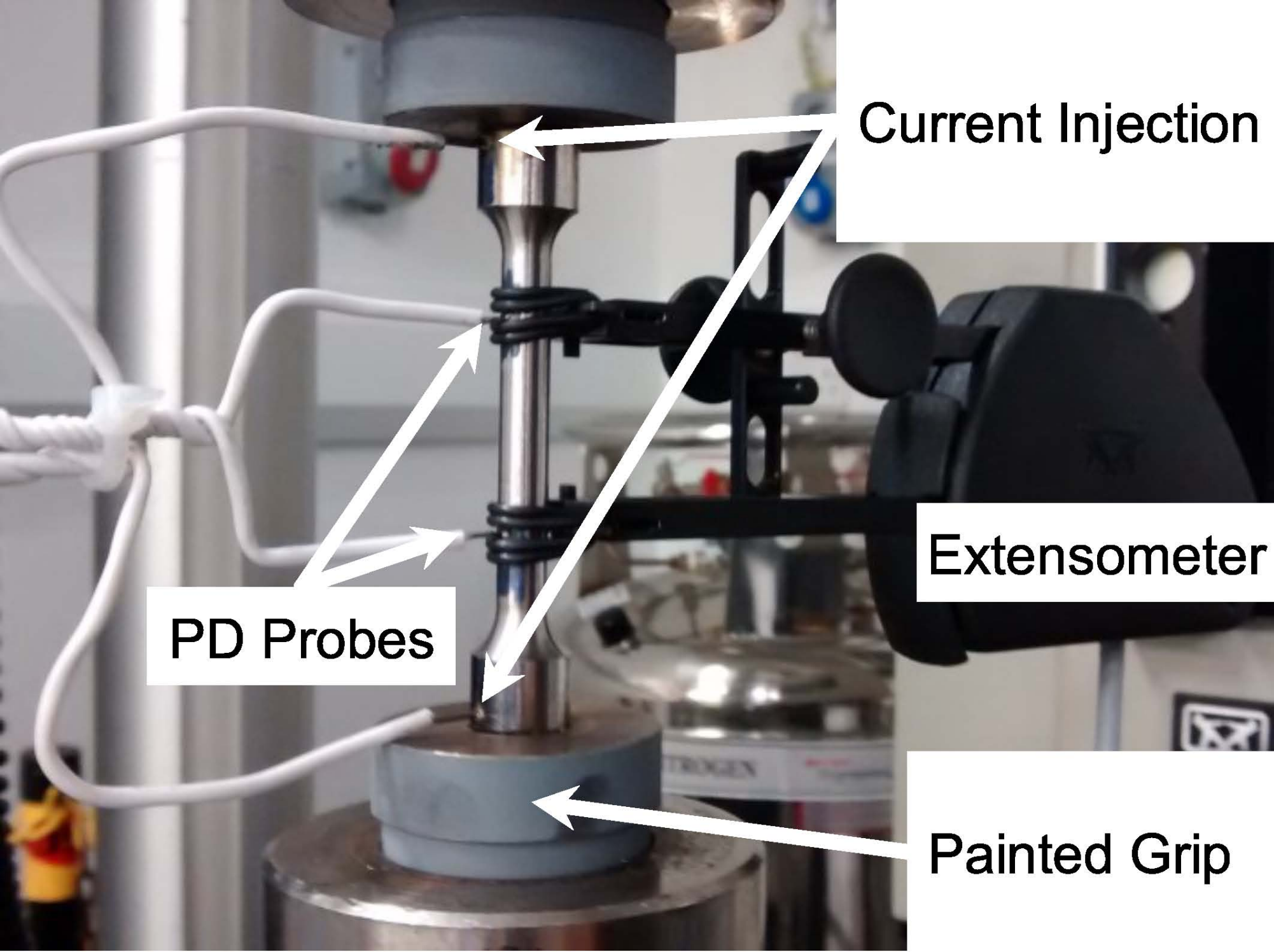
Current Injection
Extensometer
PD Probes
Painted Grip

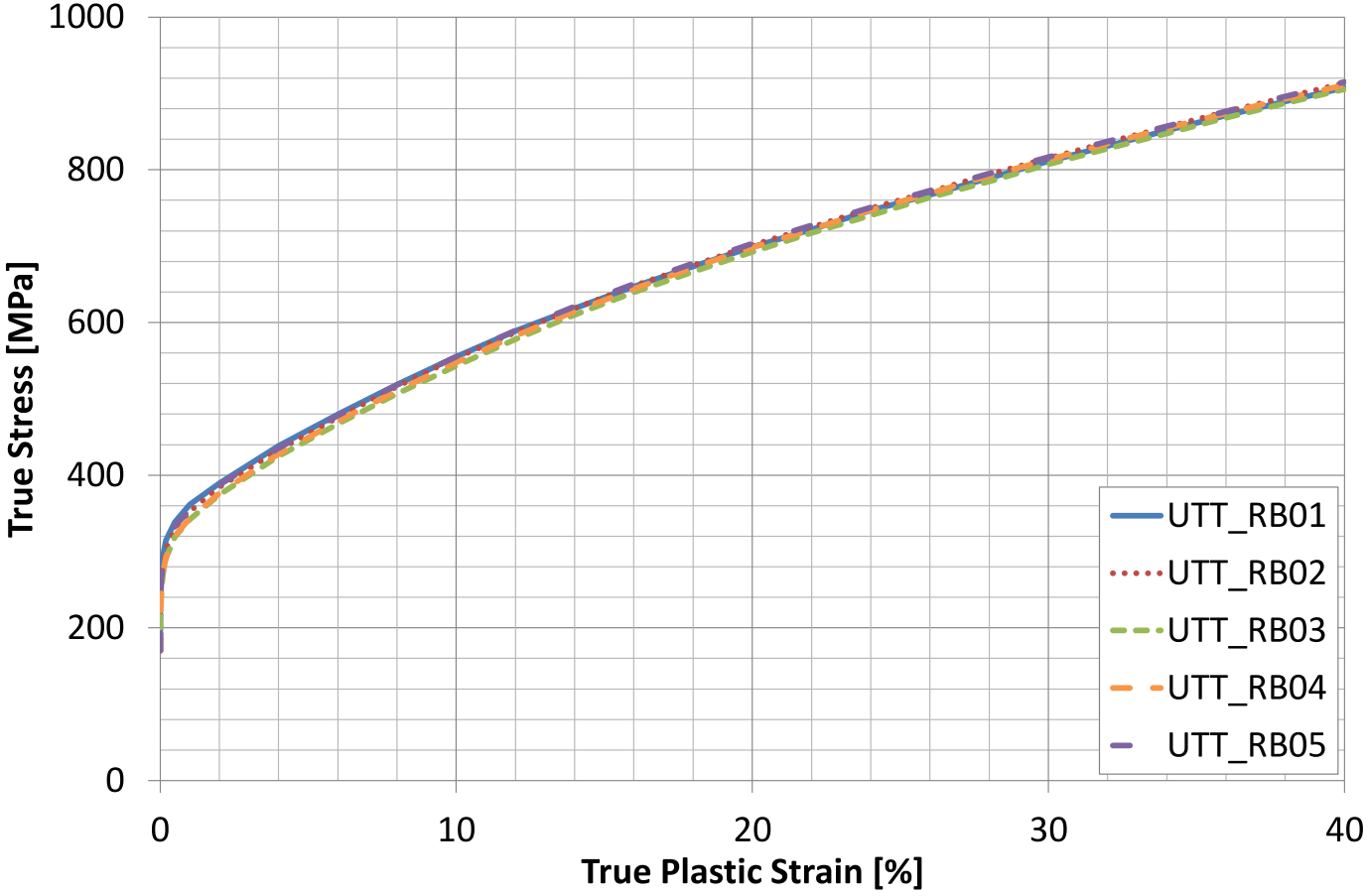
1000
800
600
400
200
0
True Stress [MPa]
0
10
20
30
40
True Plastic Strain [%]
UTT_RB01
UTT_RB02
UTT_RB03
UTT_RB04
UTT_RB05

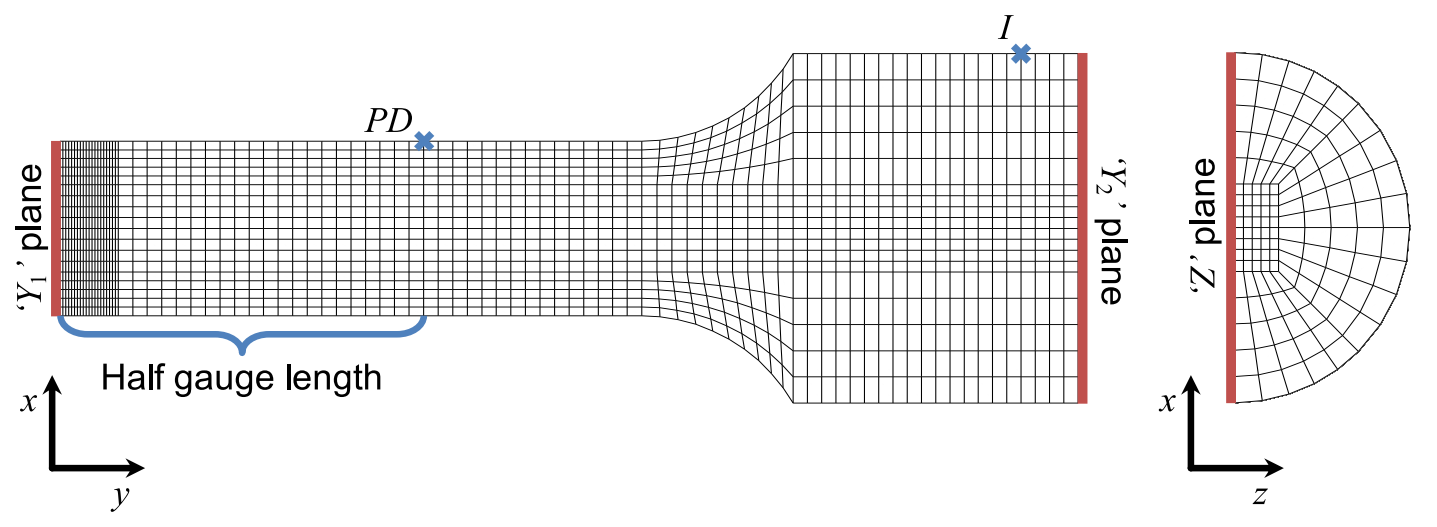
I
PD
'Y1' plane
'Y2' plane
'Z' plane
Half gauge length
x
y
x
z

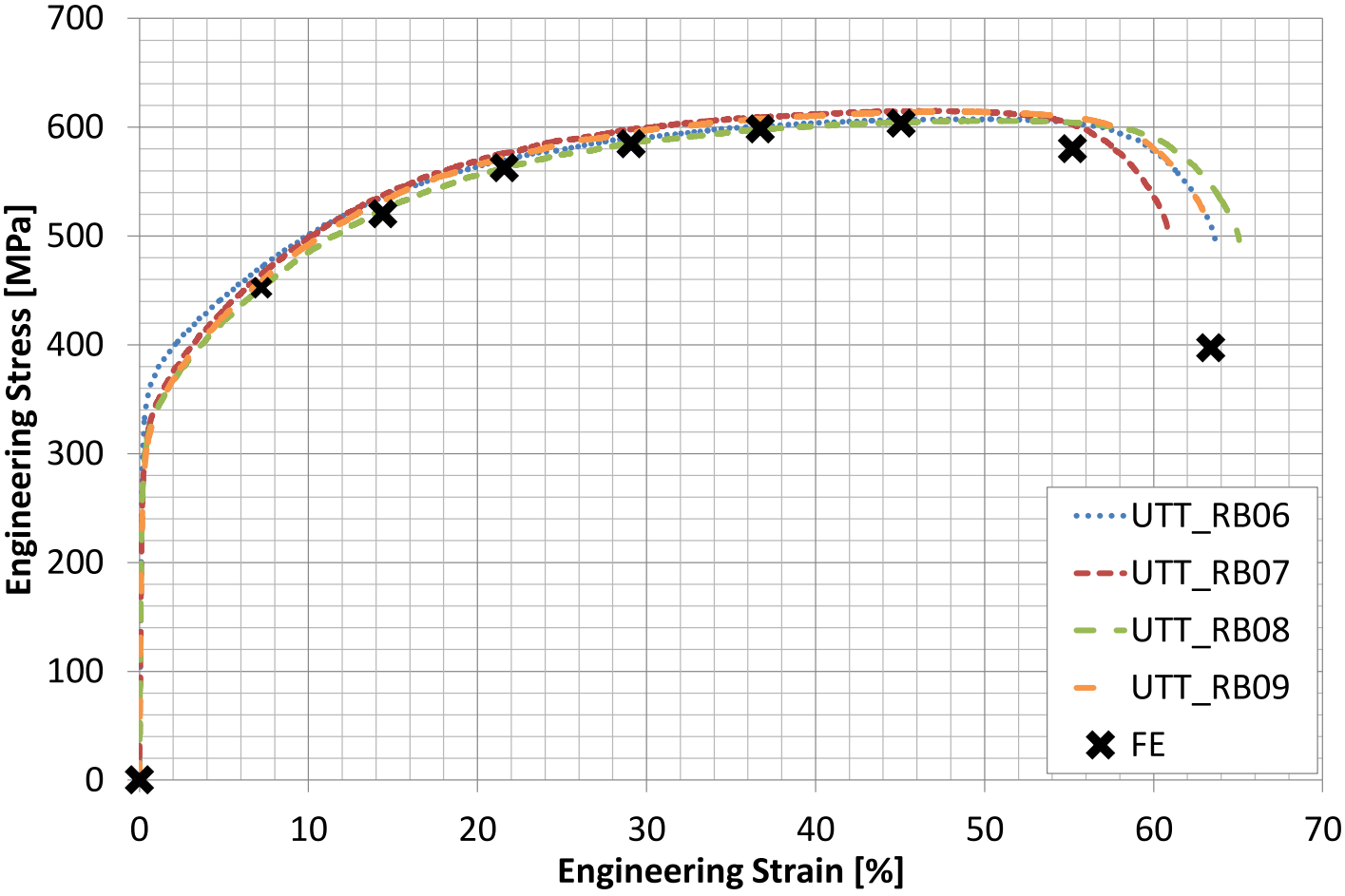
700
600
500
400
300
200
100
0
Engineering Stress [MPa]
0
10
20
30
40
50
60
70
Engineering Strain [%]
UTT_RB06
UTT_RB07
UTT_RB08
UTT_RB09
FE

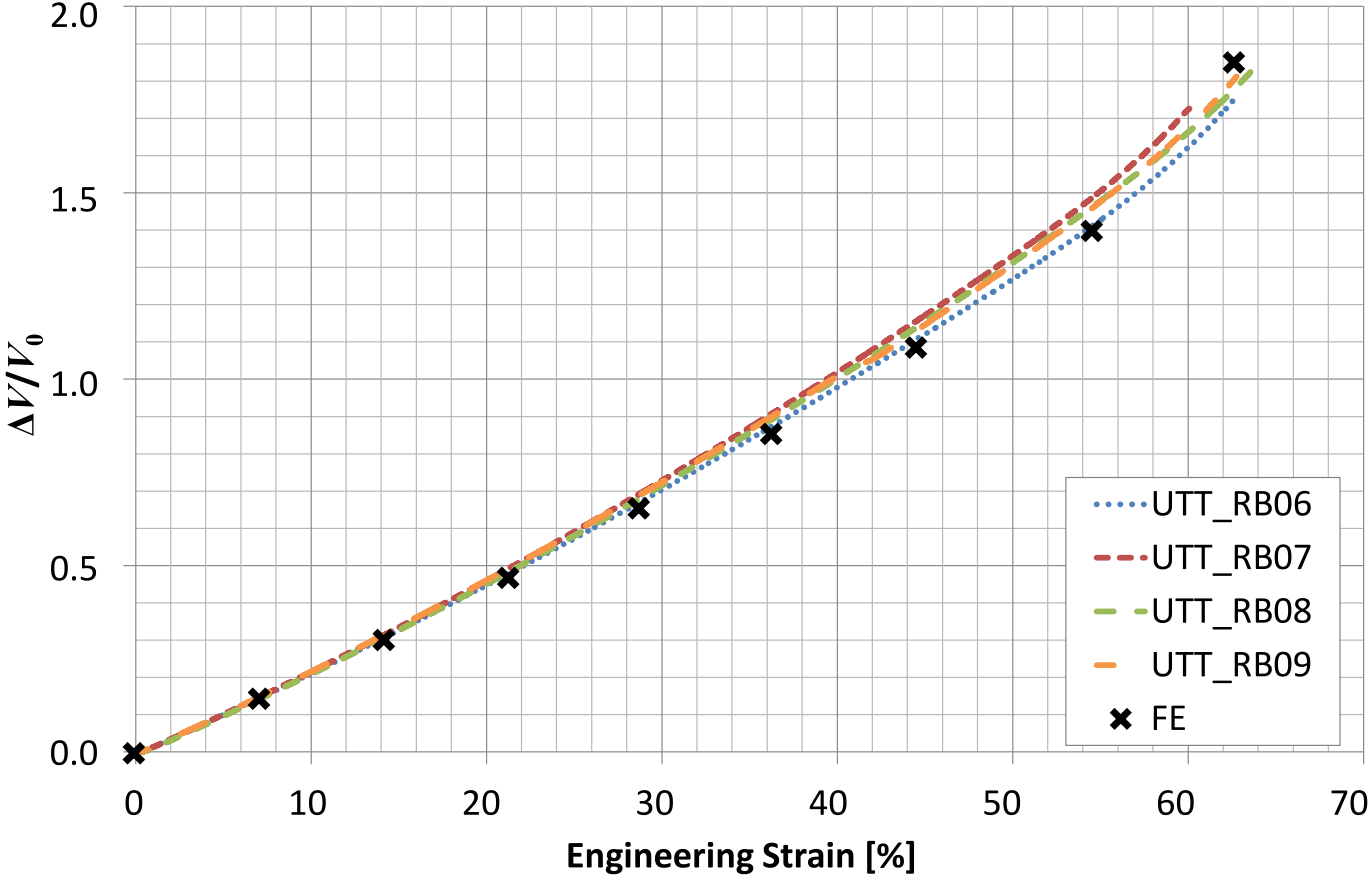
2.0
1.5
1.0
0.5
0.0
$\Delta V/V_0$
0
10
20
30
40
50
60
70
Engineering Strain [%]
UTT_RB06
UTT_RB07
UTT_RB08
UTT_RB09
FE

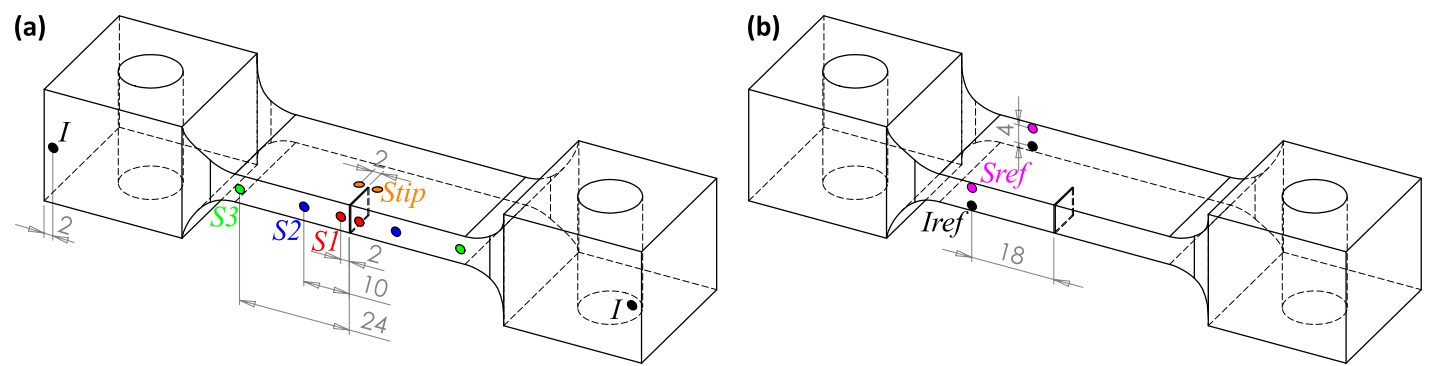
(a)
I
2
S3
S2
S1
2
Stip
2
10
24
I
(b)
4
Sref
Iref
18

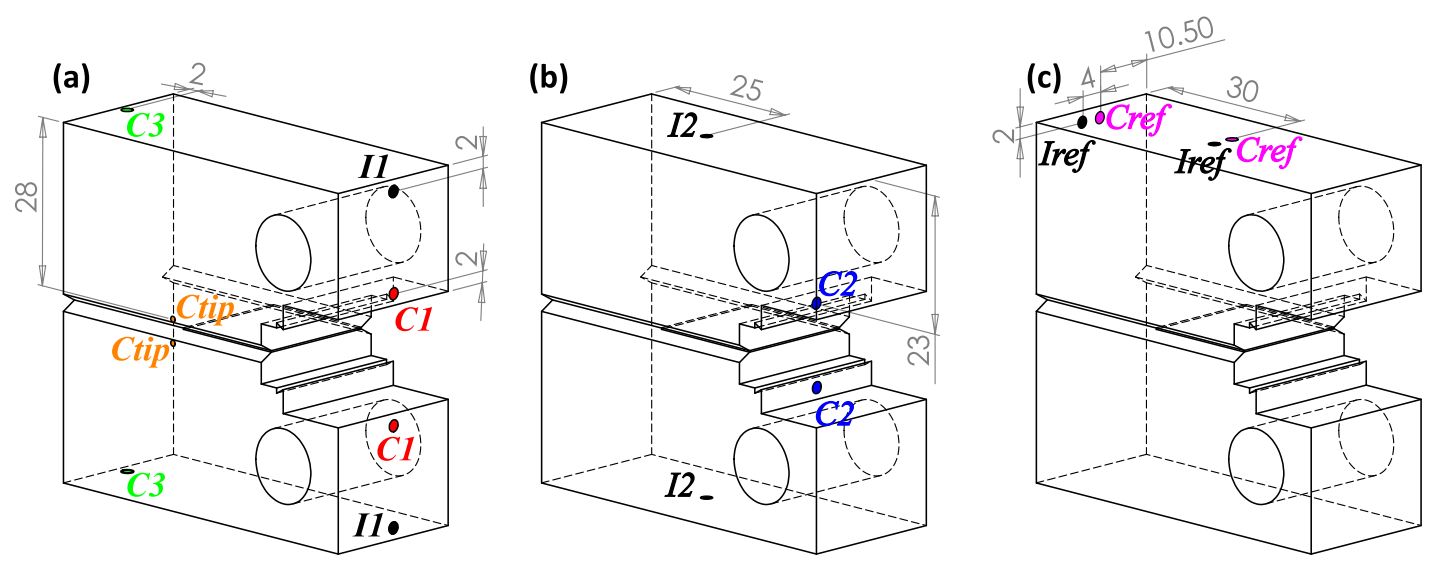
(a)
2
C3
I1
28
2
2
Ctip
C1
Ctip
C1
C3
I1
(b)
25
I2
C2
23
C2
I2
(c)
10.50
4
30
2
Cref
Iref
Iref
Cref

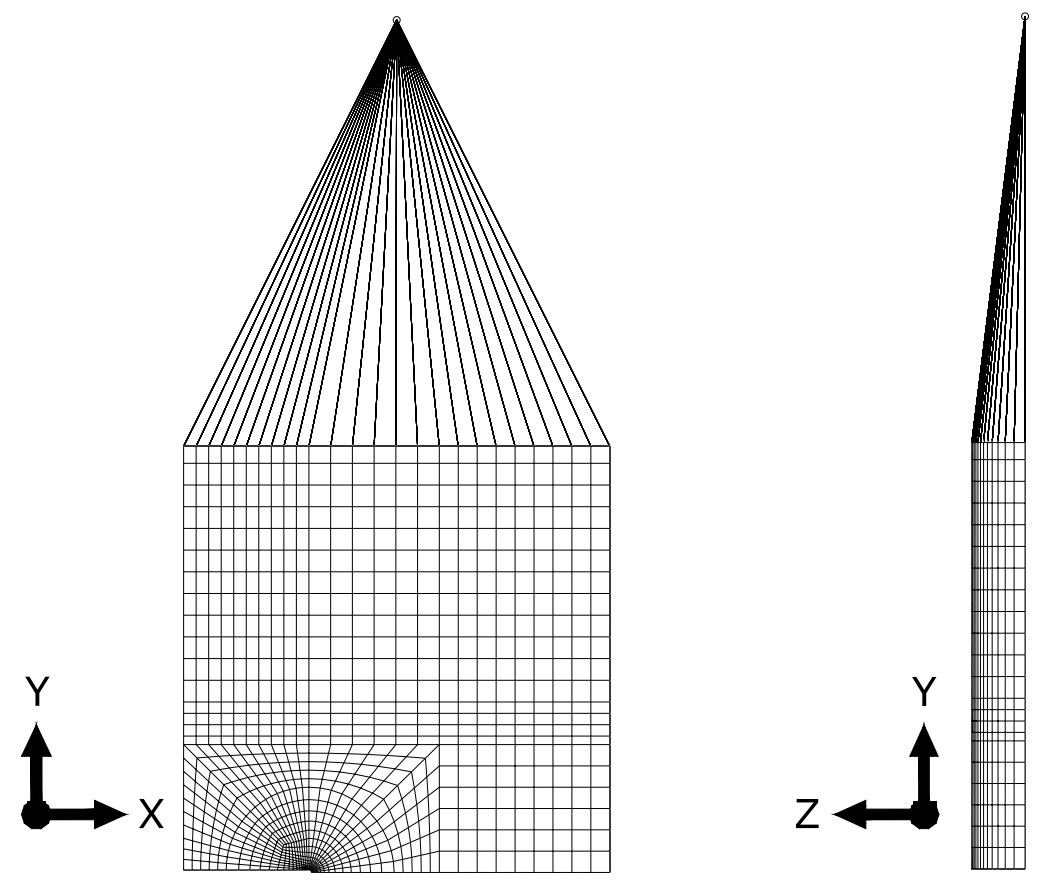
Y
X
Y
Z

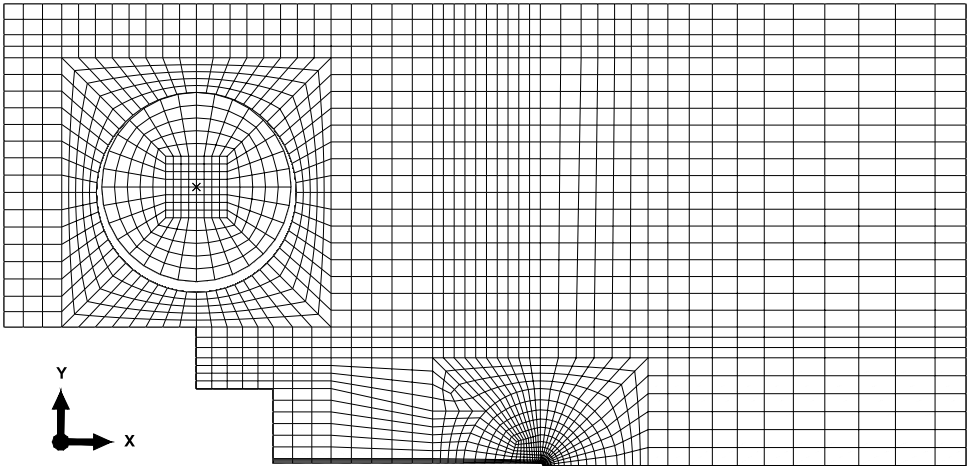
Y
X

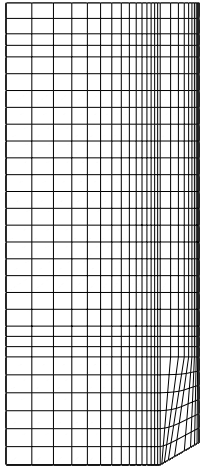
Y
Z

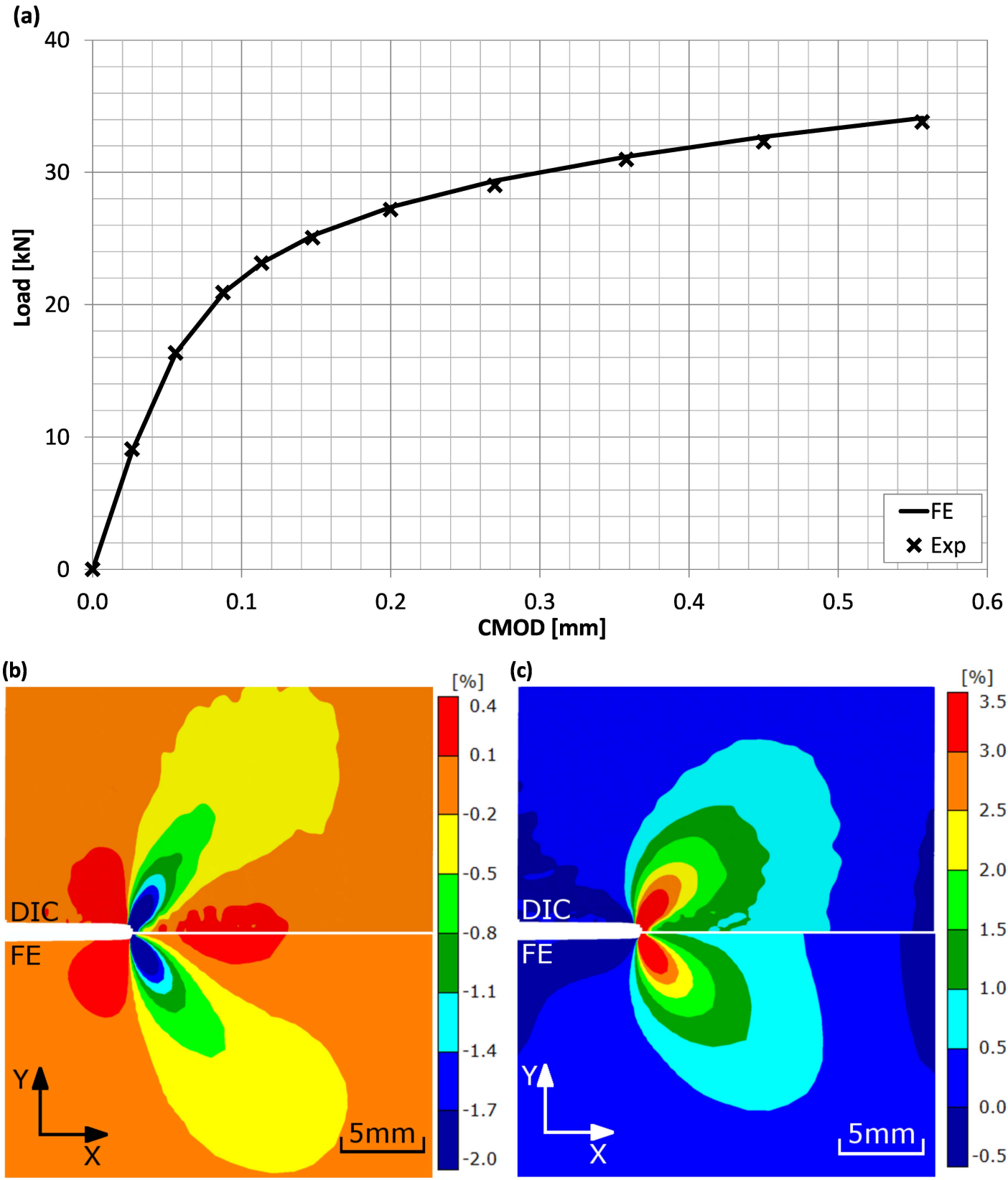
(a)
Load [kN]
CMOD [mm]
FE
Exp
(b)
DIC
FE
[%]
0.4
0.1
-0.2
-0.5
-0.8
-1.1
-1.4
-1.7
-2.0
Y
X
5mm
(c)
DIC
FE
[%]
3.5
3.0
2.5
2.0
1.5
1.0
0.5
0.0
-0.5
Y
X
5mm

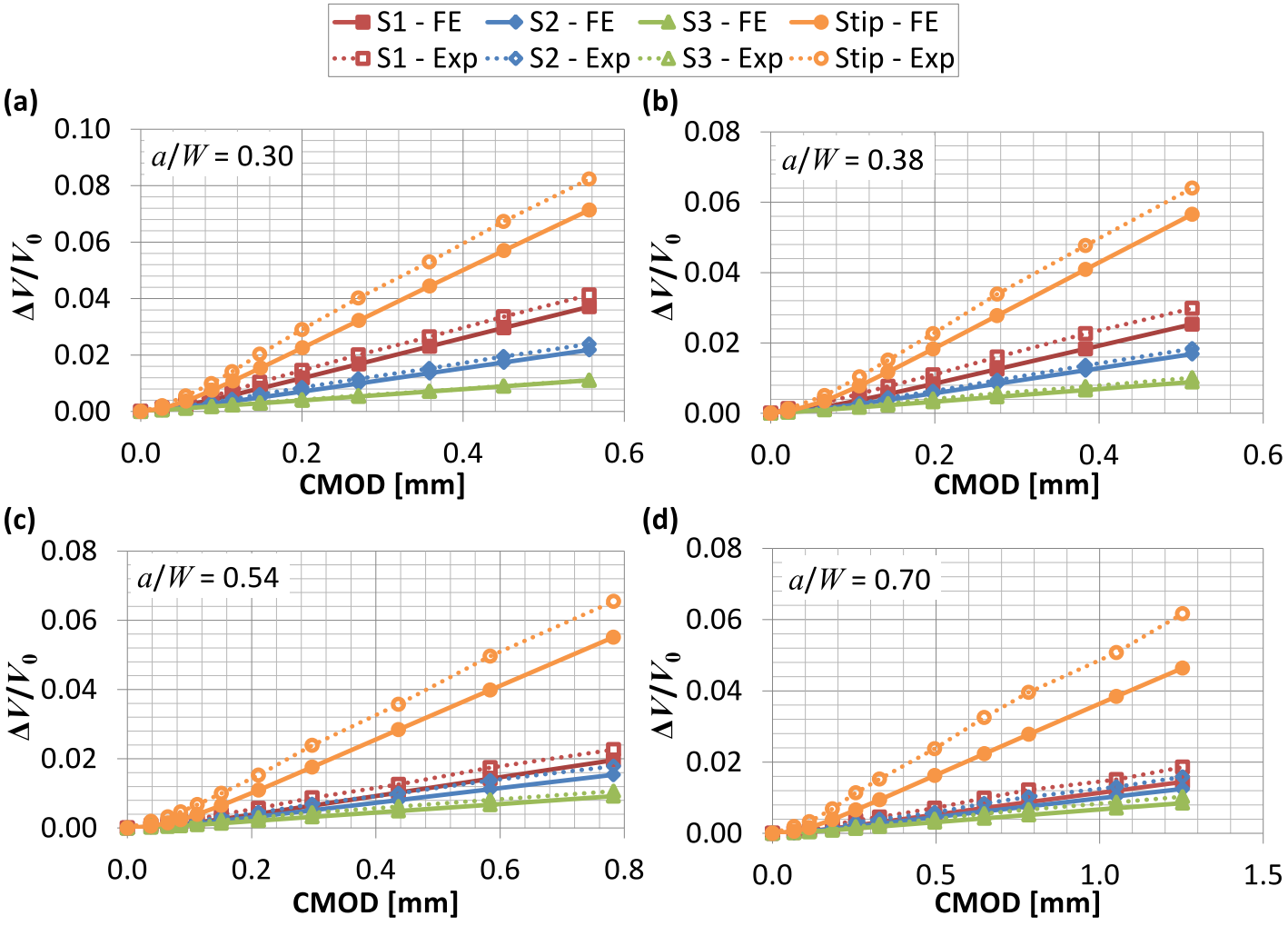
S1 - FE
S2 - FE
S3 - FE
Stip - FE
S1 - Exp
S2 - Exp
S3 - Exp
Stip - Exp
(a)
a/W = 0.30
ΔV/V0
CMOD [mm]
(b)
a/W = 0.38
ΔV/V0
CMOD [mm]
(c)
a/W = 0.54
ΔV/V0
CMOD [mm]
(d)
a/W = 0.70
ΔV/V0
CMOD [mm]

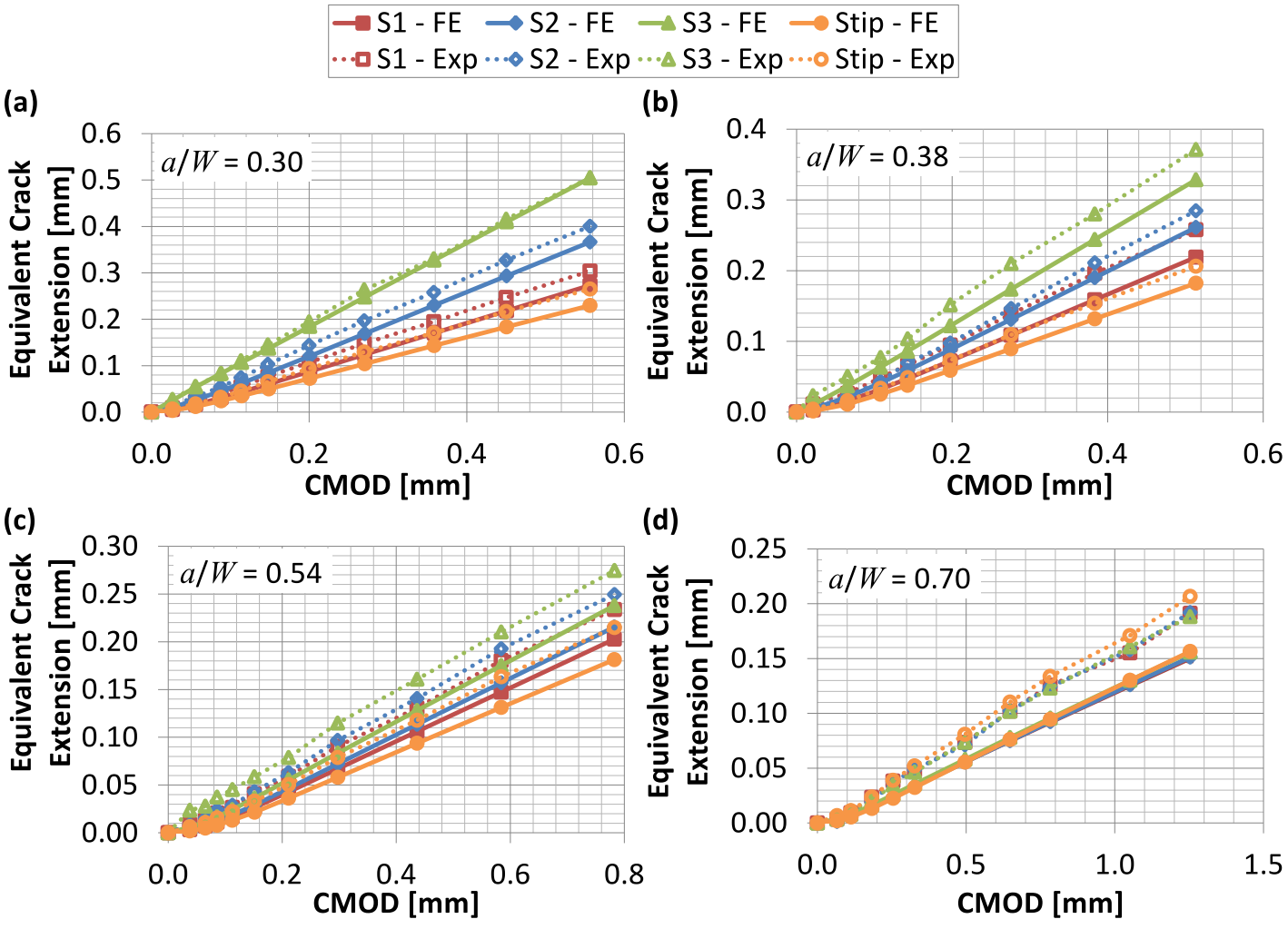
S1 - FE
S2 - FE
S3 - FE
Stip - FE
S1 - Exp
S2 - Exp
S3 - Exp
Stip - Exp
(a)
a/W = 0.30
Equivalent Crack Extension [mm]
CMOD [mm]
(b)
a/W = 0.38
Equivalent Crack Extension [mm]
CMOD [mm]
(c)
a/W = 0.54
Equivalent Crack Extension [mm]
CMOD [mm]
(d)
a/W = 0.70
Equivalvent Crack Extension [mm]
CMOD [mm]

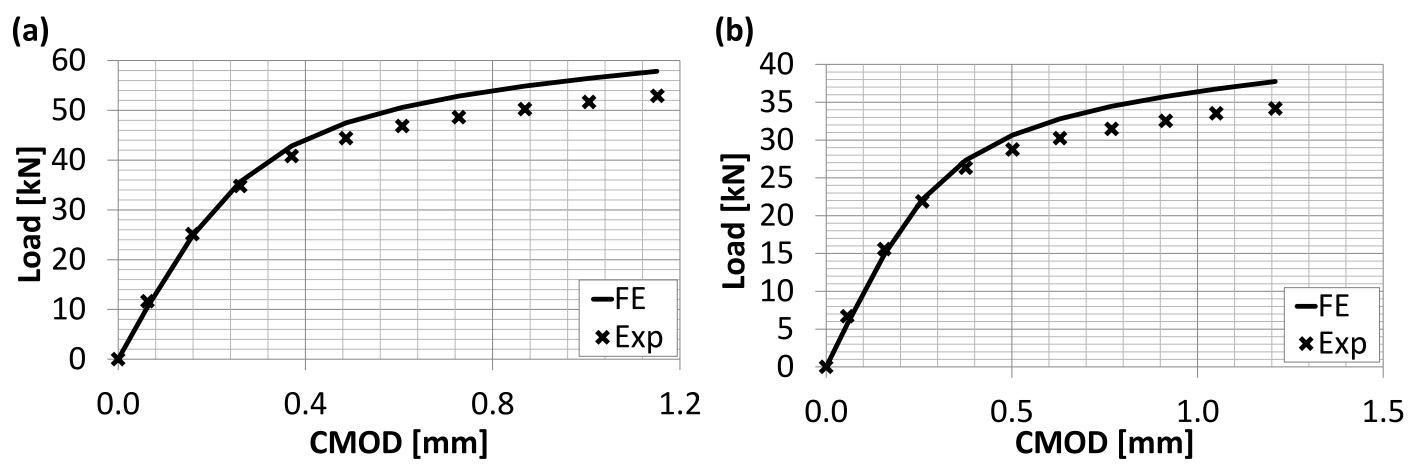
(a)
Load [kN]
60
50
40
30
20
10
0
0.0
0.4
0.8
1.2
CMOD [mm]
FE
Exp
(b)
Load [kN]
40
35
30
25
20
15
10
5
0
0.0
0.5
1.0
1.5
CMOD [mm]
FE
Exp

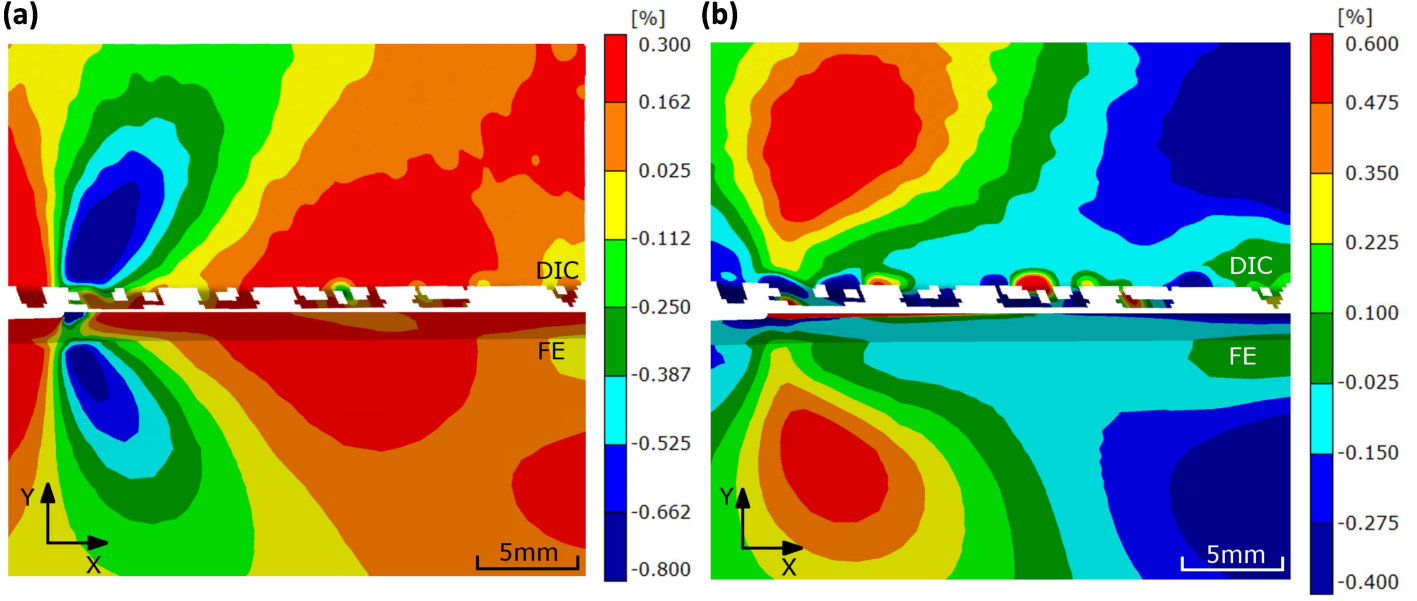
(a)
[%]
0.300
0.162
0.025
-0.112
-0.250
-0.387
-0.525
-0.662
-0.800
DIC
FE
Y
X
5mm
(b)
[%]
0.600
0.475
0.350
0.225
0.100
-0.025
-0.150
-0.275
-0.400
DIC
FE
Y
X
5mm

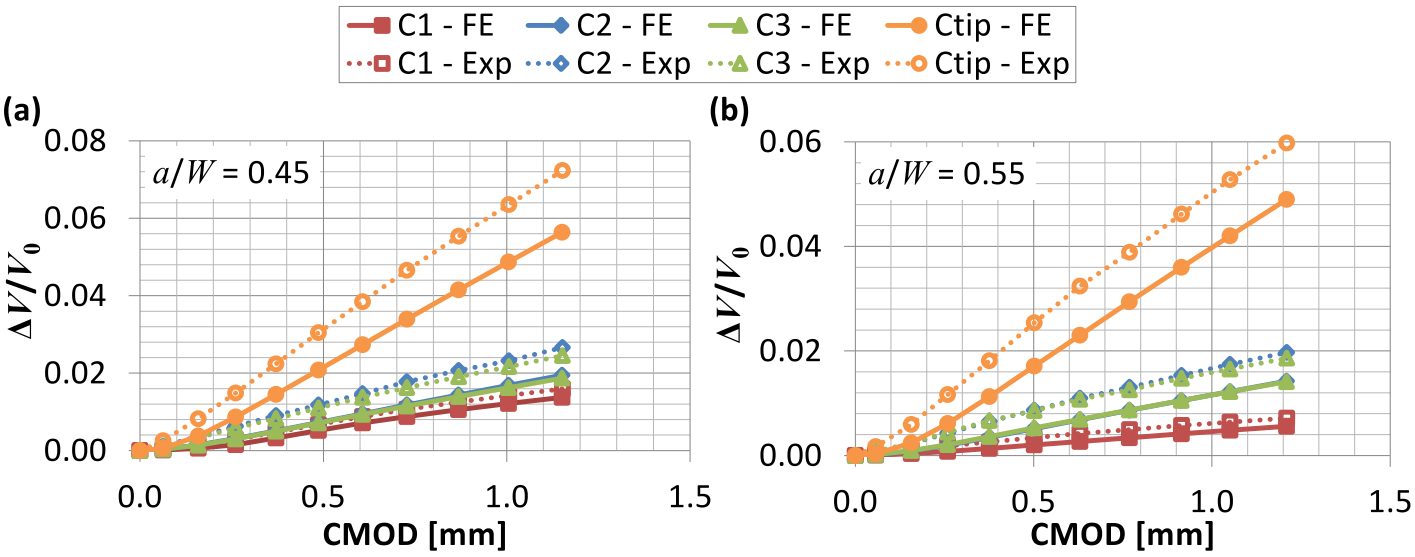
C1 - FE
C2 - FE
C3 - FE
Ctip - FE
C1 - Exp
C2 - Exp
C3 - Exp
Ctip - Exp
(a)
a/W = 0.45
ΔV/V0
0.08
0.06
0.04
0.02
0.00
0.0
0.5
1.0
1.5
CMOD [mm]
(b)
a/W = 0.55
ΔV/V0
0.06
0.04
0.02
0.00
0.0
0.5
1.0
1.5
CMOD [mm]

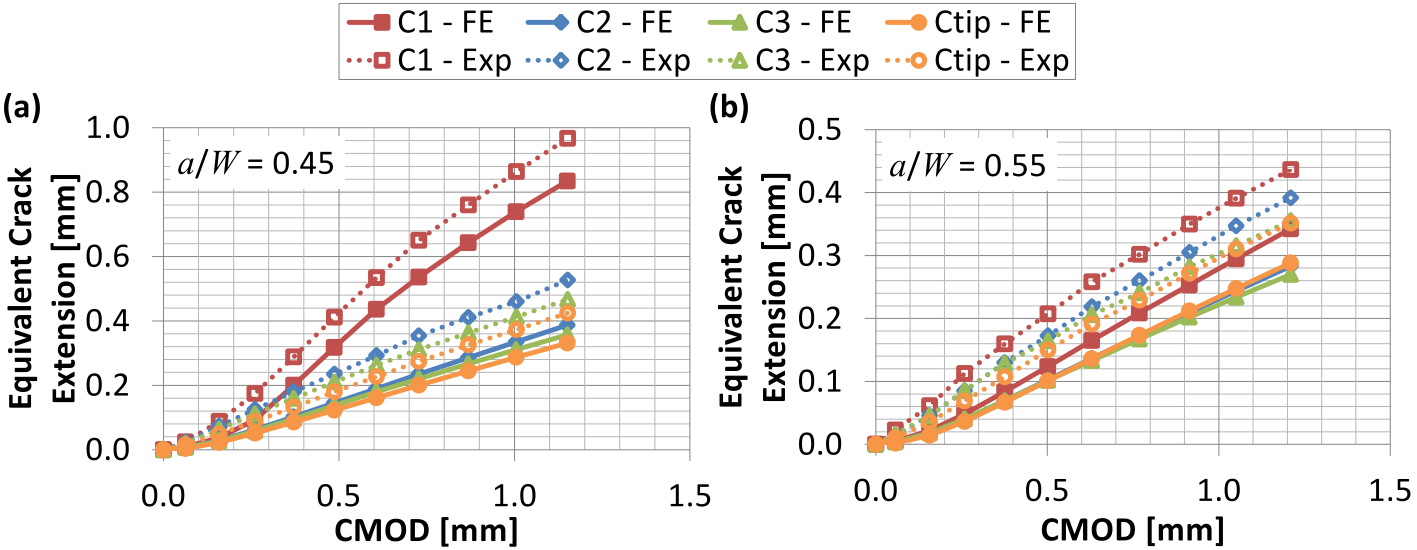
C1 - FE
C2 - FE
C3 - FE
Ctip - FE
C1 - Exp
C2 - Exp
C3 - Exp
Ctip - Exp
(a)
a/W = 0.45
Equivalent Crack Extension [mm]
CMOD [mm]
(b)
a/W = 0.55
Equivalent Crack Extension [mm]
CMOD [mm]

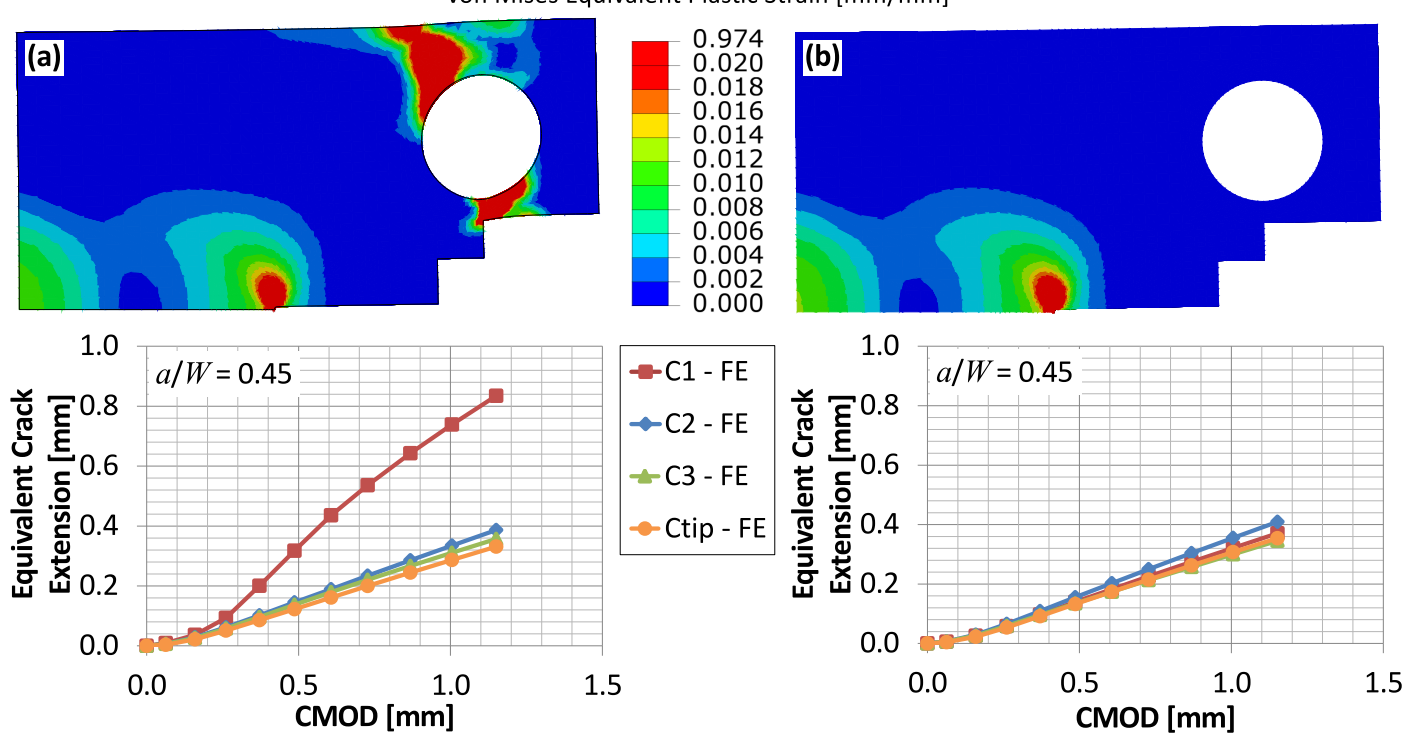
von Mises Equivalent Plastic Strain [mm/mm]
(a)
(b)
0.974
0.020
0.018
0.016
0.014
0.012
0.010
0.008
0.006
0.004
0.002
0.000
a/W = 0.45
Equivalent Crack Extension [mm]
CMOD [mm]
C1 - FE
C2 - FE
C3 - FE
Ctip - FE
a/W = 0.45
Equivalent Crack Extension [mm]
CMOD [mm]

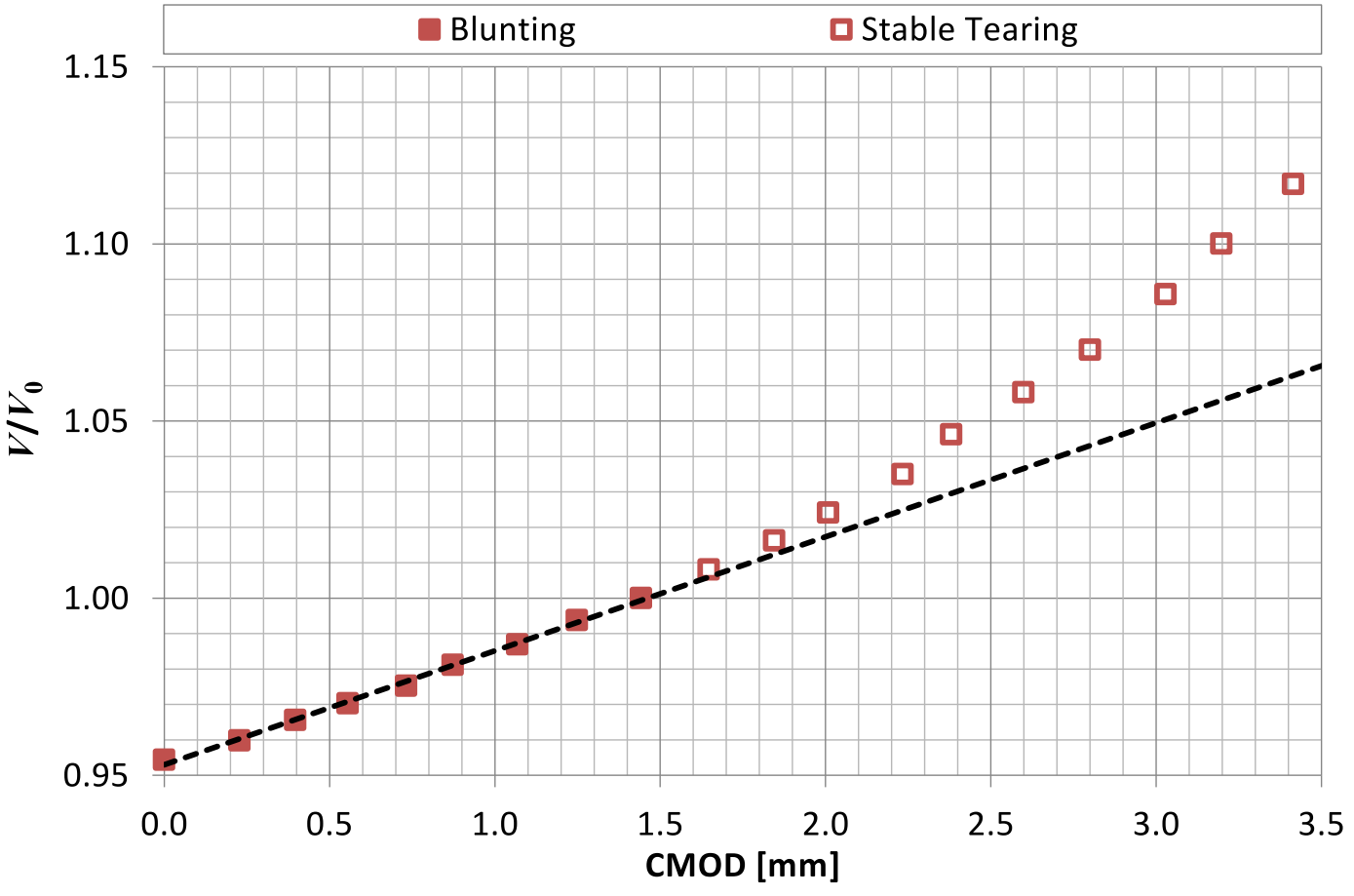
Blunting
Stable Tearing
1.15
1.10
1.05
1.00
0.95
V/V0
0.0
0.5
1.0
1.5
2.0
2.5
3.0
3.5
CMOD [mm]

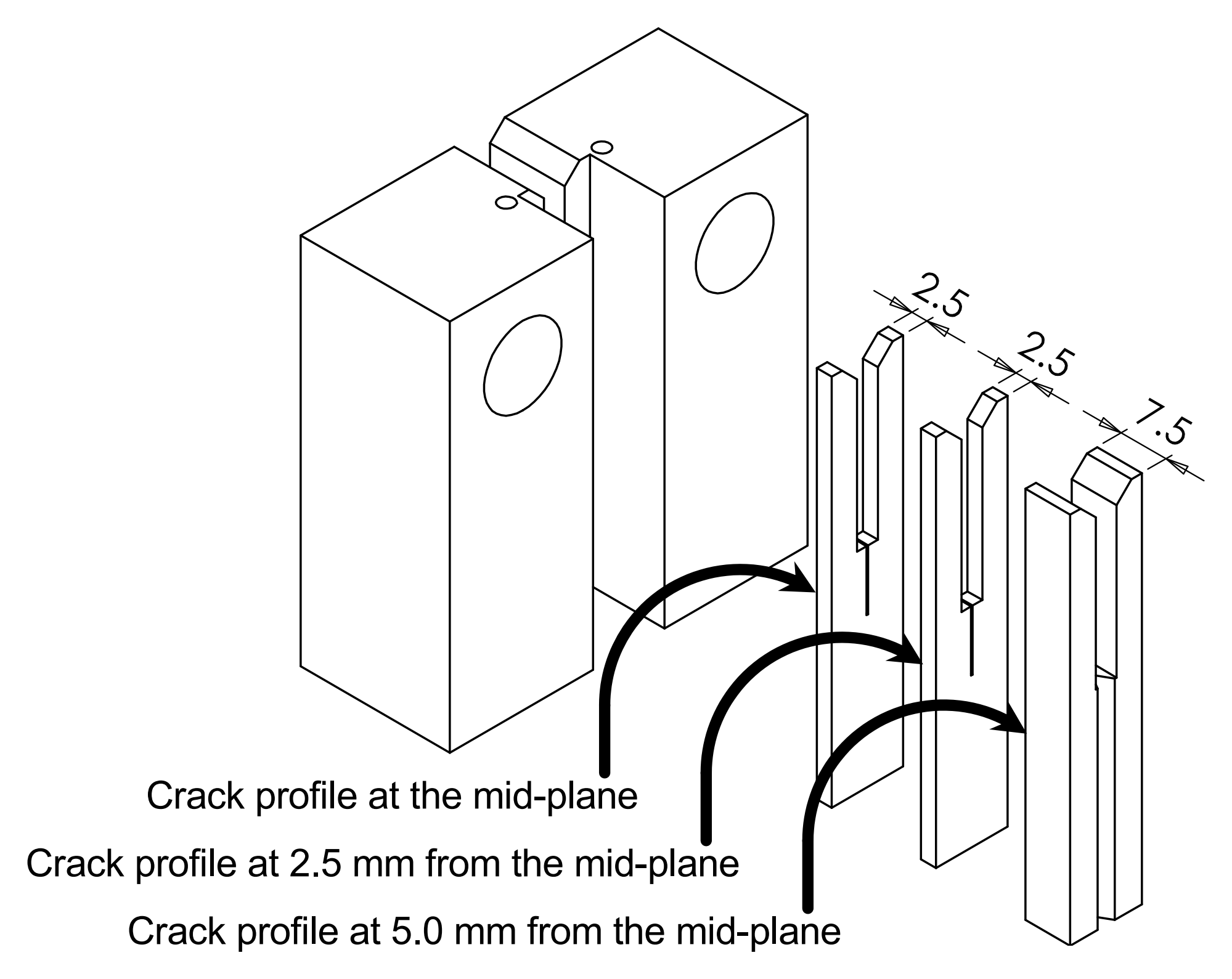
2.5
2.5
1.5
Crack profile at the mid-plane
Crack profile at 2.5 mm from the mid-plane
Crack profile at 5.0 mm from the mid-plane

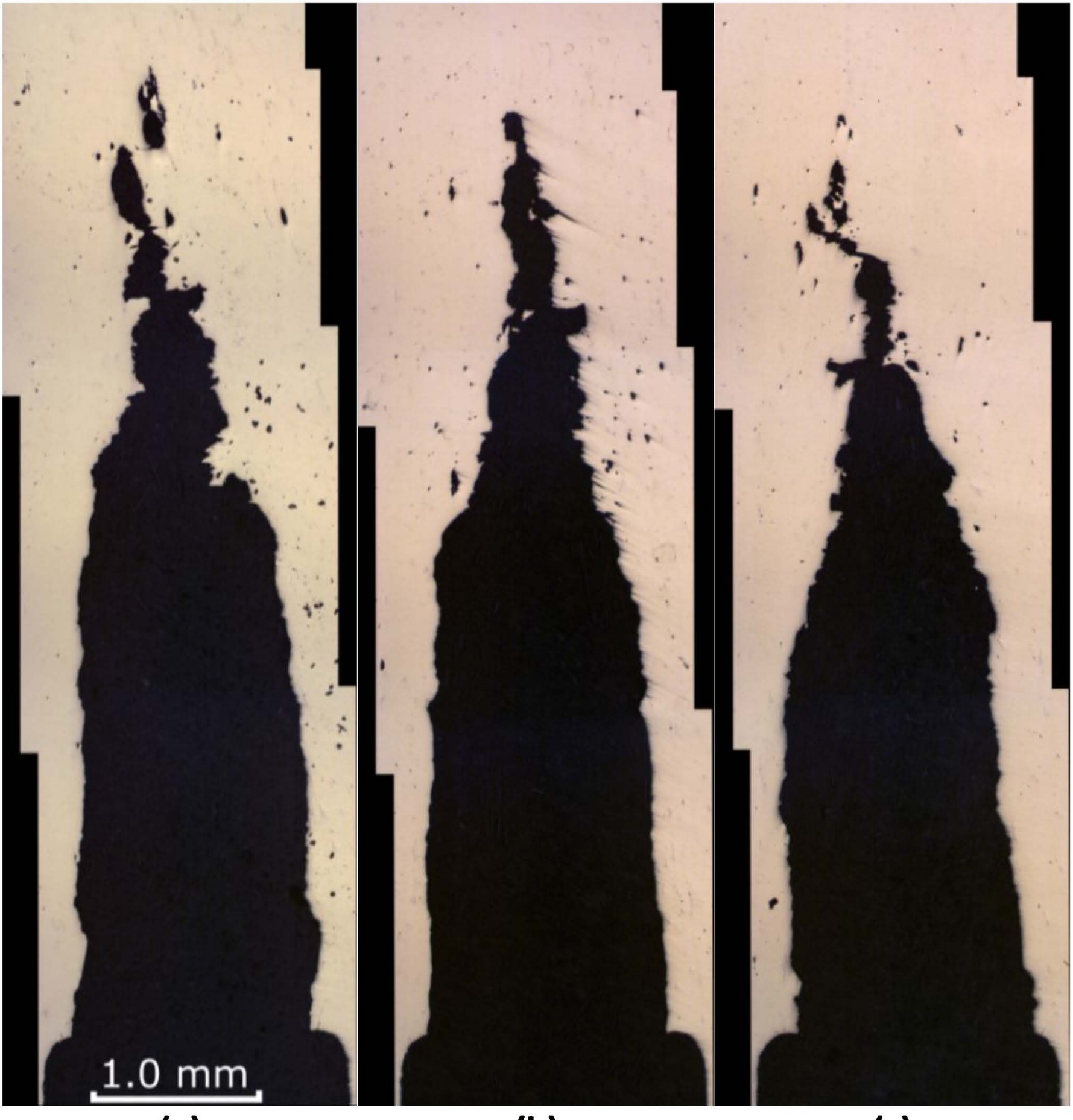
1.0 mm
(a)
(b)
(c)

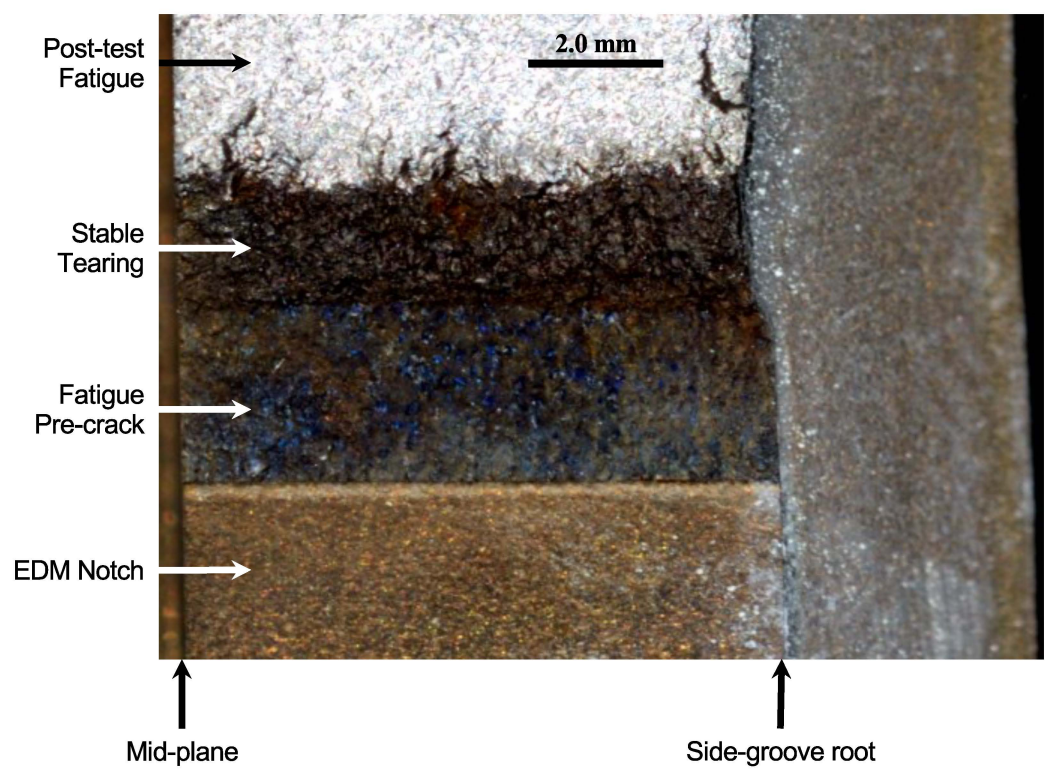
Post-test
Fatigue
2.0 mm
Stable
Tearing
Fatigue
Pre-crack
EDM Notch
Mid-plane
Side-groove root

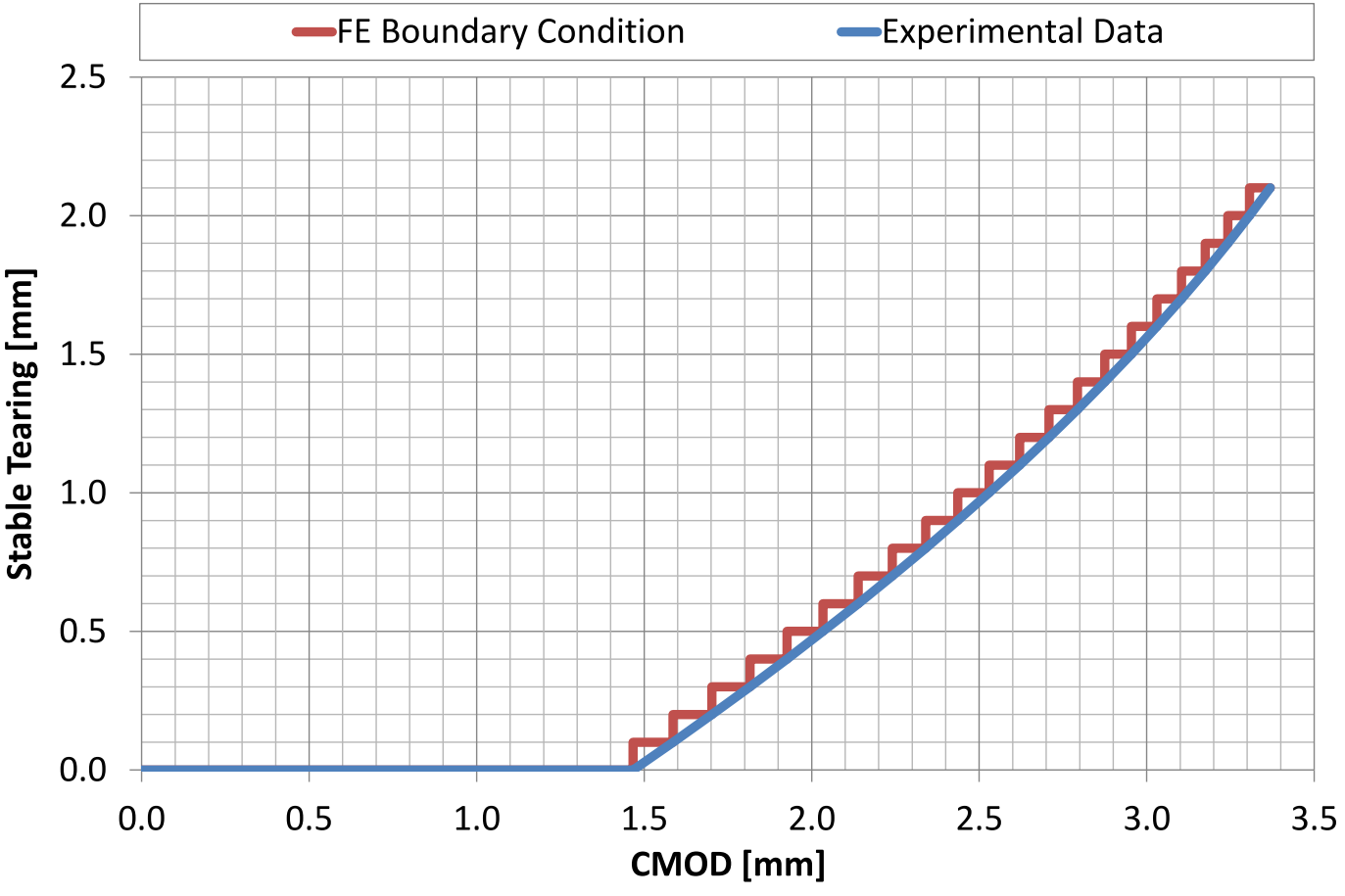
FE Boundary Condition
Experimental Data
Stable Tearing [mm]
2.5
2.0
1.5
1.0
0.5
0.0
0.0
0.5
1.0
1.5
2.0
2.5
3.0
3.5
CMOD [mm]

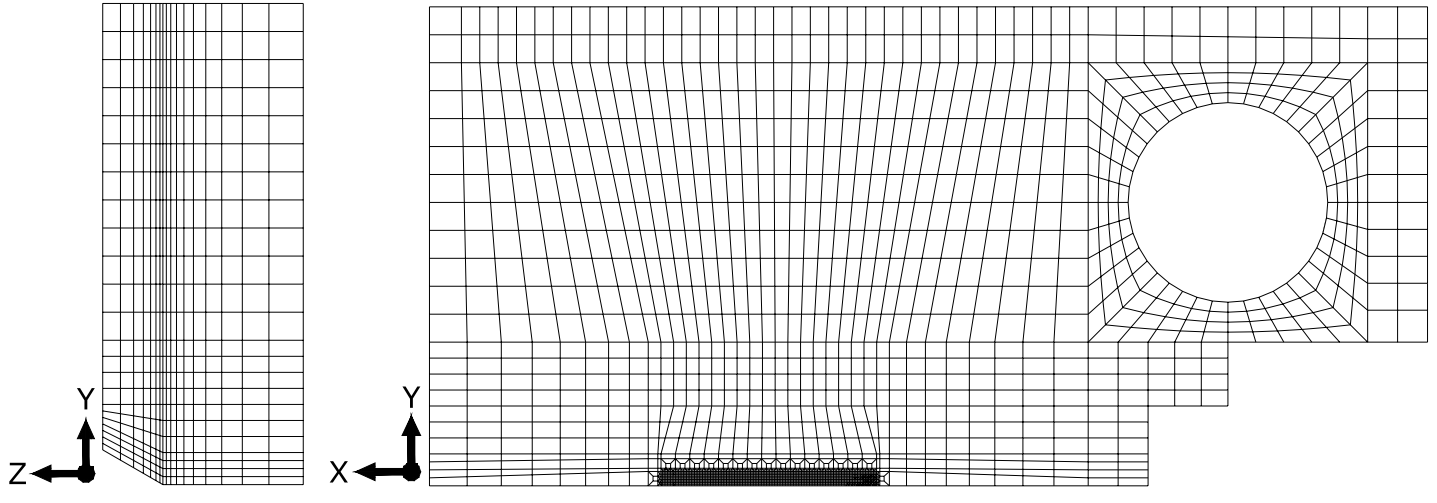
Y
Z
Y
X

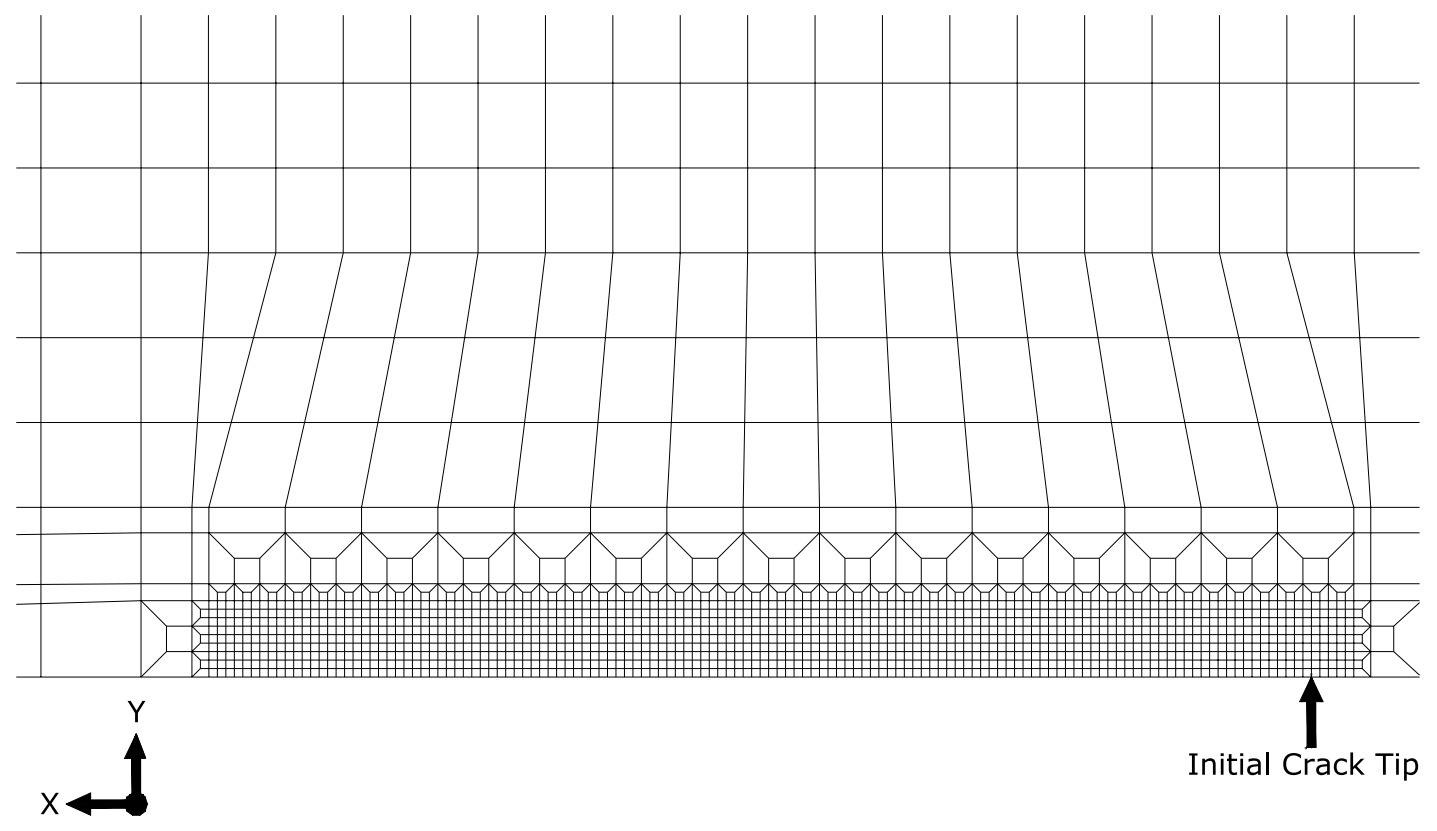
Y
X
Initial Crack Tip

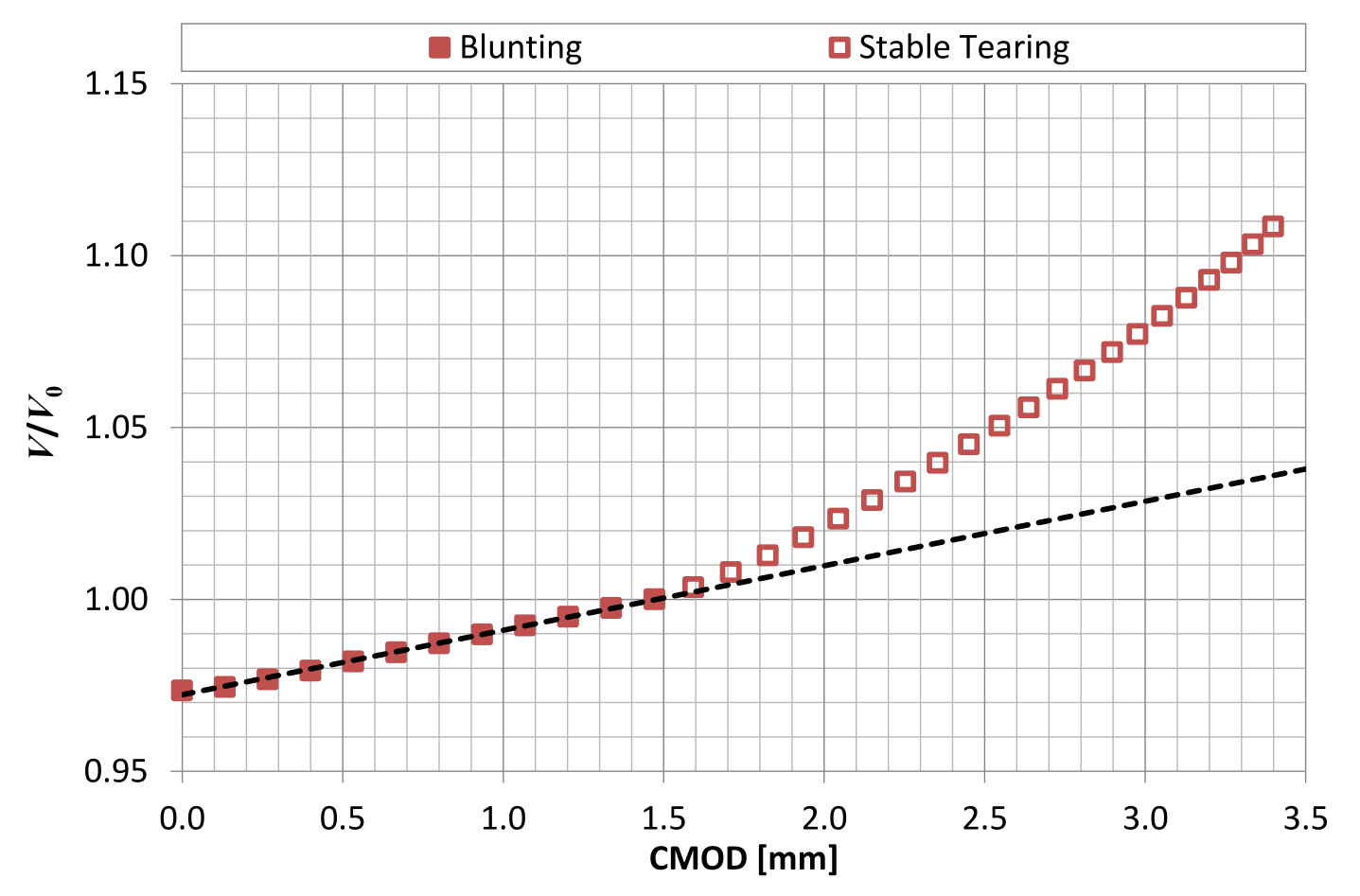
Blunting
Stable Tearing
1.15
1.10
1.05
1.00
0.95
V/V0
0.0
0.5
1.0
1.5
2.0
2.5
3.0
3.5
CMOD [mm]

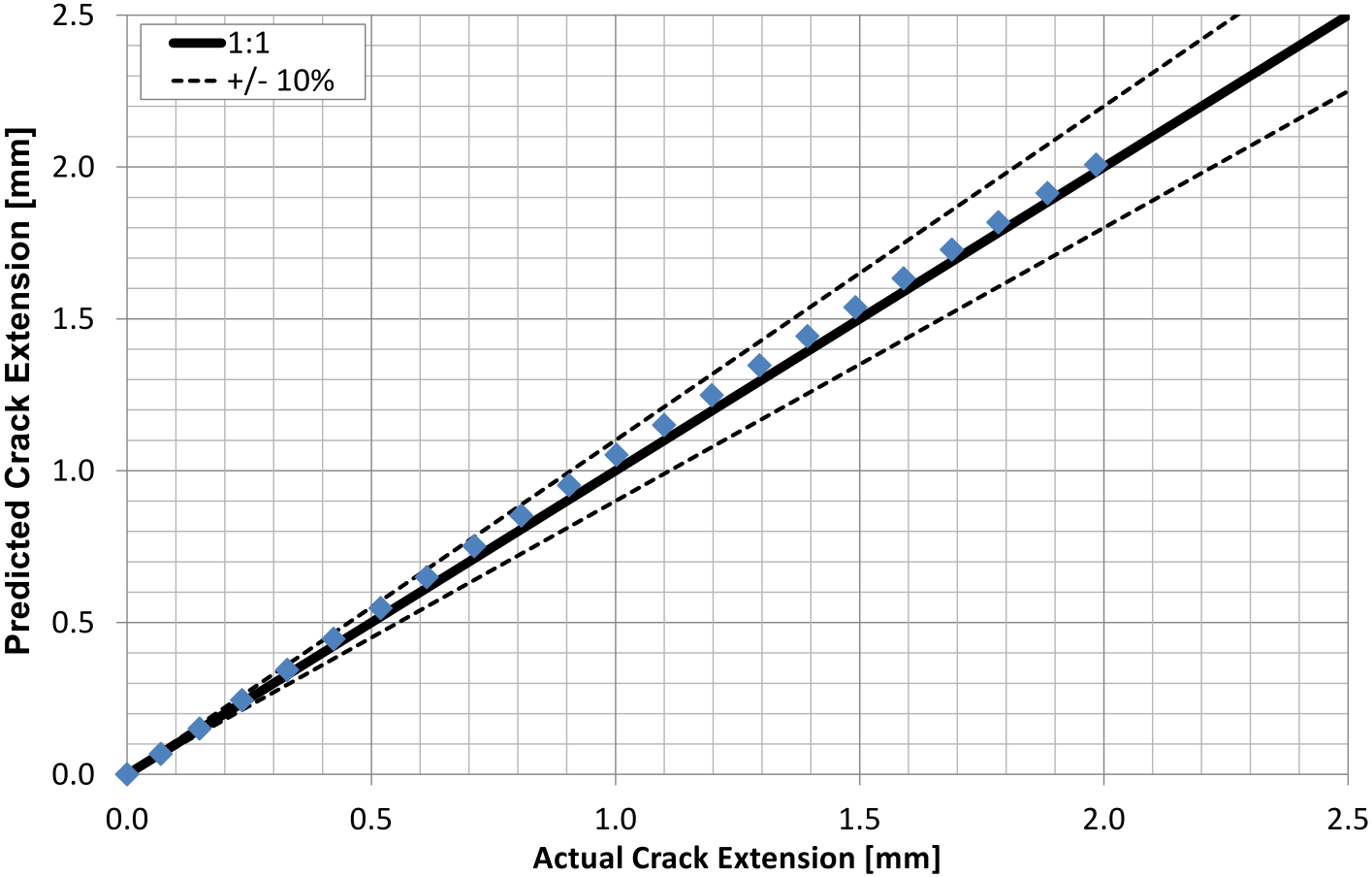
1:1
+/- 10%
Predicted Crack Extension [mm]
Actual Crack Extension [mm]
0.0
0.5
1.0
1.5
2.0
2.5